Abrupt changes in the rate of Andean Plateau uplift from reversible jump Markov Chain Monte Carlo inversion of river profiles

Matthew Fox [a,b,*], Thomas Bodin [a], David L. Shuster [a,b]

[a] Department of Earth and Planetary Science, University of California, Berkeley, CA, USA
[b] Berkeley Geochronology Center, Berkeley, CA, USA

ABSTRACT

Knowledge of the rate of surface uplift of the central Andean Plateau provides important boundary conditions for regional geodynamic models and paleoclimate reconstructions. Here we present a fully nonlinear inverse method to extract the rock uplift history of the central Andean Plateau from the Cotahuasi River and its tributaries. Our approach is based on an analytical solution to the stream power model that relates elevation to rock uplift history under the assumptions of constant climatic conditions in space and time and spatially invariant rock uplift. We use a Bayesian framework that allows us to quantify the full state of knowledge of model parameters (i.e., uncertainties, trade-offs). The erosional efficiency defines the landscape response time, and this must be determined using independent data. Therefore, using thermochronometric data from the Cotahuasi–Ocoña Canyon, which record rapid fluvial incision at ~13–10 Ma, we calibrate our results to infer a rock uplift history for the north-central Andean Plateau. We infer a pulse of rock uplift between 25 and 10 Ma at rates as high as 0.25 km/My. However, the rock uplift rate inferred during this pulse is not as high as is predicted if the central Andean Plateau grew as a result of loss of unstable lithospheric mantle. Therefore, our results are more consistent with models requiring gradual uplift of the central Andean Plateau.

© 2015 Elsevier B.V. All rights reserved.

1. Introduction

Constraining the surface uplift history of the central Andean Plateau is important for discriminating between regional geodynamic models (Barnes and Ehlers, 2009). Surface uplift through large pulses of rock uplift (<1 km over a few million years) has been proposed as indication of loss of unstable lithospheric mantle (Houseman et al., 1981) or lower crustal flow (Husson and Sempere, 2003). Conversely, lower but steady rates of rock uplift over tens of millions of years support models that invoke removal of dense lower lithosphere through continuous processes such as ablative subduction (Pope and Willett, 1998) or through continuous crustal thickening (e.g., Reiners et al., 2014). Paleoaltimetry estimates (summarized in Garzione et al., 2014) obtained from oxygen isotopes of precipitation (Garzione et al., 2006), leaf physiognomy (Gregory-Wodzicki, 2002), and Δ47 paleothermometry (Ghosh et al., 2006; Garzione et al., 2014) suggest that a rapid pulse of 2 km of surface uplift occurred between 16 and 13 Ma in the southern Altiplano and ~7 My later to the north, which appear inconsistent with continuous ablative subduction. However, because each of these surface uplift proxies depends on critical assumptions that are not easily verified, independent estimates of surface uplift provide tests of these findings.

Large rivers have cut deep canyons through the western margin of the central Andean Plateau across southwestern Peru (Fig. 1A). Modern negligible erosion rates (<0.001–0.05 mm/y) are observed at high elevations and on canyon interfluves in northern Chile (Kober et al., 2007), and thermochronometric data support little exhumation (<2 km) on the Central Andean Plateau since ~60 Ma (Schildgen et al., 2007). Therefore surface uplift is approximately equal to rock uplift and the elevation of the plateau constrains close to the total amount of rock uplift. In turn, the onset of incision of these canyons provides minimum constraints on the onset of surface uplift. Cotahuasi–Ocoña Canyon is the deepest canyon, reaching depths of 3 km below the plateau surface (Fig. 1B). One approach to constrain the timing of canyon incision is to obtain radiometric ages of volcanic deposits that drape topography. Such deposits found <400 m above the modern river indicate that the canyon had almost reached its present depth by 2–4 Ma (Schildgen et al., 2007; Thouret et al., 2007). An alternative approach to measure canyon incision is to exploit thermochronometric methods that record cooling as the present-day bedrock approached Earth's surface. This approach suggests that the onset of incision of the central section of the canyon was approximately 13–10 Ma (Schildgen et al., 2009, 2010). In turn, the onset of incision provides a minimum age for the onset of surface uplift.

Additional constraints on Andean uplift history may be provided through the analysis of functional dependencies that map the input of

---

* Corresponding author. Tel.: +1 510 644 0225.
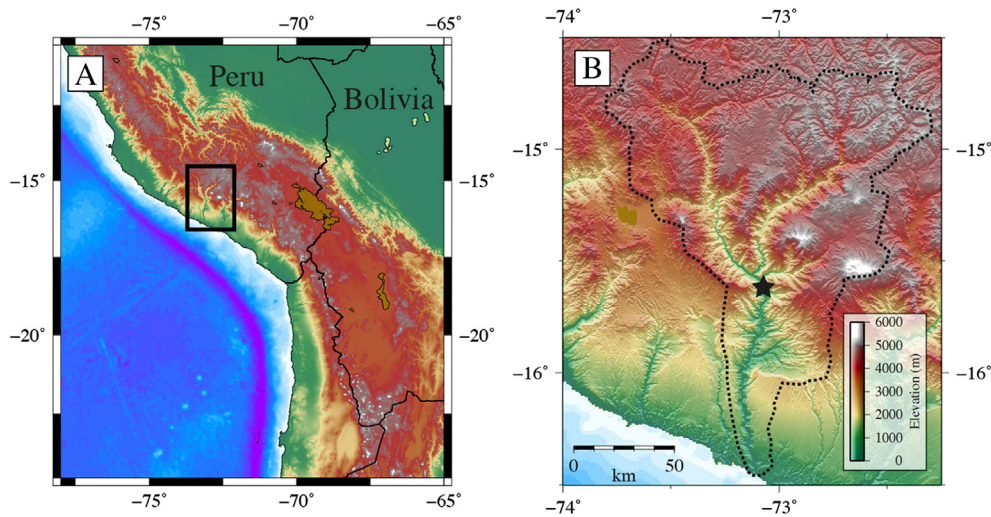 *E-mail address:* matthew.fox@berkeley.edu (M. Fox).

Fig. 1. (A) Topography of the central Andean Plateau showing the location of the Cotahuasi–Ocoña Canyon. (B) Topography of the study region. The dotted black curve shows the approximate outline of the Cotahuasi–Ocoña catchment. The star shows the location of the thermochronometric data used to calibrate the rock uplift rate history. Data source: SRTM topographic data (Jarvis et al., 2006).

rock uplift to the output of topography (Whipple and Tucker, 1999; Kirby et al., 2003; Whittaker et al., 2007; Kirby and Whipple, 2012; Roberts et al., 2012; Jeffery et al., 2013; Goren et al., 2014). Therefore, the topography 'records' the forms and magnitudes of the rock uplift rate history, provided independent data exist that can calibrate this record (Davis, 1899; Penck et al., 1972). A number of approaches have been developed to extract rock uplift rate information from topography based on a stream power model in which erosion is a function of the local channel slope, upstream drainage area, and bedrock erodibility (Howard, 1994). A potential limitation of this approach is that changes in climate associated with surface uplift of the Andean Plateau, leading to temporal and spatial variations in precipitation (Insel et al., 2010; Poulsen et al., 2010), may have played an important role in modulating fluvial incision of the Cotahuasi–Ocoña catchment (Jeffery et al., 2013). However, the dependence of erosion rates on precipitation across the Andean Plateau remains debated (Hilley and Coutand, 2010; Norton and Schlunegger, 2011; Gasparini and Whipple, 2014; Whipple and Gasparini, 2014).

Here we present a fully nonlinear inverse method to extract a rock uplift history from digital elevation data of river channels, combined with geological constraints. Our approach is based on an analytical solution to the stream power model that relates modern elevation to past changes in rock uplift history (Royden and Perron, 2013; Goren et al., 2014), and we use a Bayesian framework that allows us to quantify the full state of knowledge of model parameters. The erosional efficiency (Howard and Kerby, 1983) defines the landscape response time, and this erosional efficiency is not 'contained' in the current topography. Therefore, we use published thermochronometric data from the Cotahuasi–Ocoña catchment, which record rapid fluvial incision at ~13–10 Ma (Schildgen et al., 2010), to calibrate our results. This empirical calibration ultimately quantifies changes in rock uplift through time for the north-central Andean Plateau. In this contribution, we first provide a brief description of previous work that has focused on extracting tectonic signals from fluvial topography. We then describe the forward model and our inverse approach to quantify permissible rock uplift rate histories. As an initial test of our inverse approach and to highlight the suitability of our method, we apply our approach to the Inyo Mountain range in the western Basin and Range, USA, which has a well-constrained rock uplift history (Goren et al., 2014). We then present the extracted drainage network for the Cotahuasi–Ocoña catchment and a rock uplift history for this part of the Central Andean Plateau. Finally, we assess the effects of changes in climate on our inferred history with a synthetic example.

2. Extracting tectonics from river profiles using the stream power model

In the stream power model, erosion rate is parameterized as a function of: (i) the slope of a river profile dz/dx, where z is the surface elevation and x is distance along the channel; (ii) the discharge that is parameterized as a function of the upstream drainage area, A; and (iii) the erosional efficiency, K, that accounts for lithology, climatic conditions, sediment flux, and hydraulic parameters. Using this parameterization, the evolution of a detachment-limited fluvial channel is expressed as

$$\frac{\partial z(t,x)}{\partial t} = u(t,x) - KA^m \left(\frac{\partial z(t,x)}{\partial x} \right)^n \tag{1}$$

where t is time and $u(t,x)$ is the rate of tectonic rock uplift. The exponents m and n are positive constants, and the appropriate values are debated (Howard and Kerby, 1983; Seidl and Dietrich, 1992; Tucker and Slingerland, 1994; Whipple and Tucker, 1999; Attal et al., 2008; Whittaker and Boulton, 2012).

Eq. (1) is an advection equation (Rosenbloom and Anderson, 1994) and, the response time for information to propagate from the base level, at $x = 0$, to a point x upstream is

$$\tau(x) = \int_0^x \frac{dx'}{KA(x')^m S(x')^{n-1}}. \tag{2}$$

The most commonly used technique to infer rock uplift rate from topography is an analysis of the relationship between slope and drainage area, leading to a steepness index (Flint, 1974), k_s, that represents the ratio of the rock uplift rate to erosional efficiency (Whipple and Tucker, 1999; Snyder et al., 2000; Kirby et al., 2003; Schoenbohm et al., 2004; DiBiase et al., 2010; Kirby and Whipple, 2012). Calculating slopes from a digital elevation model, however, accentuates noise (Cohen et al., 2008; Perron and Royden, 2013; Mudd et al., 2014); and to increase the signal-to-noise ratio, information from multiple pixels must be averaged leading to reduced resolution.

A more robust approach to extract uplift rate history is to exploit analytical solutions to the stream power model (Luke, 1972, 1974, 1976; Weissel and Seidl, 1998; Harkins et al., 2007; Pritchard et al., 2009; Royden and Perron, 2013), as slope is not required. However, the erosional efficiency term, K, determines the rate at which a

landscape responds to a change in rock uplift rate — and K is often unknown. To circumvent the requirement that K be known (although assuming K is constant in space and time), Royden and Perron (2013) introduced a variable transformation for the length of a fluvial profile into a variable χ, which has units of distance but accounts for the scaling of elevation with drainage area. With this variable transformation, the analytical solution relates present-day elevation to rock uplift rate normalized by the erosional efficiency (Perron and Royden, 2013; Royden and Perron, 2013), and the slope of the χ–z relationship is proportional to k_s.

Inversion of river profiles to infer rock uplift rates was established by Roberts and White (2010) and by Roberts et al. (2012) for inferring rock uplift rates as a function of space and time. In these approaches, the stream power model is solved numerically, and parameter values defining rock uplift rates can be determined using a nonlinear inverse method. Linear inverse methods based on analytical solutions to the stream power model have also been developed (Fox et al., 2014; Goren et al., 2014). These approaches enable a greater number of elevation nodes to be analyzed simultaneously and thus increased model resolution is possible. However, these inverse methods require that the inverse problem be solved with some form of model regularization to account for geomorphic noise and the possibility of mixed determinacy. Therefore, inferred rock uplift histories are artificially forced to be smooth in time and also in space (when solving the general space–time problem). In reality, the presence of relict landscapes at high elevations separated from steeper rejuvenated landscapes by fluvial knickpoints (e.g. Whipple and Tucker, 1999; Bishop et al., 2005; Berlin and Anderson, 2007) highlights that alternative methods may be required to infer nonsmooth changes in rock uplift rate.

Mudd et al. (2014) developed a statistical framework to identify the location of fluvial knickpoints based on the χ–elevation relationships (Perron and Royden, 2013; Royden and Perron, 2013). In this approach, a linear segment is regressed through a χ–elevation relationship, and the locations of knickpoints can be chosen at random. In order to prevent the selection of a complex model that fits every elevation node including geomorphic noise, a modified Akaike Information Criteria (AIC) (Akaike, 1974) can be minimized that favors models that fit the data well and penalizes models that are overly complex. The solution with the lowest AIC value is the favored solution. This approach, however, does not provide a statistical measure of the probability of identifying a knickpoint at a specific χ value or the slope of the χ–elevation relationship at a specific χ value. Therefore, in some cases it may be challenging to identify which parts of the solution are well resolved.

In this work, we address these issues with a transdimensional algorithm, which presents several advantages: (i) the problem is cast in a Bayesian framework with no need for explicit smoothing; (ii) the parameterization of the model is self adaptive, where the location and number of change points need not be defined in advance; and (iii) uncertainties are correctly accounted for, and one can estimate the variability in the range of possible solutions.

3. Methods

3.1. Forward model

In this section we present our approach to infer rock uplift rates from fluvial topography. Throughout this paper, we assume that $n = 1$, and incision rate is linear in the local slope (please refer to Goren et al., 2014, for a discussion on this assumption). Therefore, Eq. (2) reduces to:

$$\tau(x) = \int_0^x \frac{dx'}{KA(x')^m}. \tag{3}$$

The analytical solution for the linear version of Eq. (1) can be written as (Royden and Perron, 2013; Goren et al., 2014):

$$z(0,x) = \int_{-\tau(x)}^0 u(t')dt' \tag{4}$$

where t' is the integration parameter, $\tau(x)$ is the response time as expressed in Eq. (3).

3.2. Scaling out time through the erosional efficiency

As $\tau(x)$ is controlled by the erosional efficiency, K, which is often unknown, we assume that K is constant through time and factor K out from Eq. (4) by introducing K-scaled variables after Goren et al. (2014):

$$\chi = A_0^m K\tau \tag{5}$$

$$u^* = \frac{u}{KA_0^m} \tag{6}$$

and

$$t^* = KA_0^m t \tag{7}$$

where A_0 is an arbitrary scaling area to be consistent with the notation and dimensionality of Perron and Royden (2013). This variable transformation allows us to express topography in a K independent form:

$$z(0,x) = \int_{-\chi(x)}^0 u^*(t')dt' \tag{8}$$

where χ in Eq. (5) is defined as in Perron and Royden (2013). It has units of length, but given the kinematic wave nature of Eq. (1), it contains information on both time and space.

3.3. Inverse model

In order to tackle the inverse problem, we need an approach to parameterize the rock uplift history. We parameterize u^* as a function of t^* using a series of nodes. Each node defines the center of a Voronoi cell, and t^* positions of changes in u^* are defined at the boundaries of the Voronoi cells (where the boundary of two neighboring Voronoi cells is equidistant between the centers of the two cells), and u^* is constant within each cell. The number of nodes is variable and describes the complexity of the model. This concept is shown in Fig. 2A. Here there are five nodes describing u^* as a function of t^*, which define four knickpoints identified as changes in slope of the χ–elevation relationship (Fig. 2B). The slope of each segment of the χ–elevation relationship is equal to the u^* value in the corresponding Voronoi cell. The inverse problem is to infer the probability distribution of u^* as a function of t^* or $u^*(t^*)$.
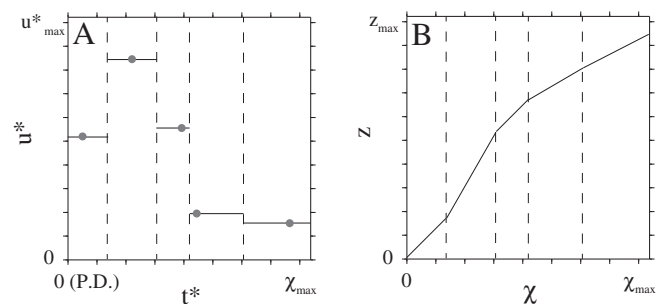

Fig. 2. (A) Parameterization of u^* as a function of t^*. The gray circles show the locations of the nodes that are used to define one-dimensional Voronoi cells. Note that the nodes are not in the center of the cells. (B) Example of predicted elevations (z) owing to the $u^*(t^*)$ function shown in (A).

Here we adopt a Bayesian probabilistic framework to propagate uncertainty associated with the elevation data and produce estimates of u^* along with uncertainties. We define two vectors to simplify the analysis. The first vector, β, contains the positions of the Voronoi cells that describe $u^*(t^*)$: $\beta = [\mathbf{u}^*, \mathbf{t}^*]$ where $\mathbf{u}^* = [u_1^*, u_2^*, ..., u_k^*]$ and $\mathbf{t}^* = [t_1^*, t_2^*, ..., t_k^*]$, where k is the number of nodes, which is variable. The second vector, α, contains the observations. In the Bayesian framework, the probability distribution of $u^*(t^*)$ we wish to approximate is termed the posterior probability distribution. Following Bayes' Theorem (Tarantola, 2005; Sivia and Skilling, 2006), the posterior probability distribution of the model parameters β given the data set α is a product of the model likelihood function (which quantifies data fit) with the prior distribution of the model parameters (which quantifies what is known about the parameters 'prior' to the analysis): the posterior density is expressed as $p(\beta|\alpha)$; the likelihood function is $p(\alpha|\beta)$; and the prior probability is $p(\beta)$. Therefore, $p(\beta|\alpha)$ is expressed as

$$p(\beta|\alpha) = Cp(\alpha|\beta)p(\beta) \tag{9}$$

where C is a constant that ensures that the posterior probability integrates to unity; $p(\beta|\alpha)$ is approximated numerically using a Markov Chain Monte Carlo (MCMC) algorithm to efficiently sample a multidimensional parameter space. The MCMC algorithm is based on a random walk that samples the space of possible models (Hastings, 1970) and will be discussed below.

In order to use a Bayesian approach, we also need to define a prior probability distribution and a likelihood function. Because we assume that all parameters are independent a priori, we can write

$$p(\beta) = \prod_{i=1}^{k} p(u_i^*) * \prod_{i=1}^{k} p(t_i^*) \tag{10}$$

and for each $p(u_i^*)$ we use a noninformative uniform prior between 0 and u_{max}^*, and for each $p(t_i^*)$ we use a noninformative uniform prior between t_{min}^* and t_{max}^*.

The likelihood function measures the probability that the predicted and observed data are consistent given a mathematical model for the random noise distribution. The form of this probability density function is given by what we think we know about uncertainties on α. We assume that the noise associated with an observed elevation node, z_o, is normally distributed with a mean of z_o and a variance σ^2. We could use the vertical error of a DEM to define σ, which can be a few meters across elevations from 0 to 6000 m. In practice, the noise term represents geomorphic noise associated with landslides, small-scale drainage divide migration, changes in lithology, a failure to accurately identify the active fluvial channel, and simplifications associated with the stream power model, which is unable to capture small-scale geomorphic features. In turn, this term describing geomorphic noise is likely to be much greater than the reported DEM precision. Given this assumption for the noise distribution, the data likelihood given the model parameters is

$$p(\beta|A) = \prod_{i=1}^{N} \frac{1}{\sigma\sqrt{2\pi}} exp\left[-\frac{1}{2}\left(\frac{z_o - z_p}{\sigma}\right)^2\right]. \tag{11}$$

Note that the level of data noise σ represents the required level of data fit and, hence, directly determines the complexity of the solution (the number of changes in rock uplift rate). Since σ accounts for the combined effects of different sources of noise that are difficult to quantify, it is also treated as an unknown parameter in the inversion to be constrained by the data. This type of approach is called hierarchical Bayes (Malinverno, 2002; Malinverno and Briggs, 2004; Bodin et al., 2012a) because it has two levels of inferences: at the higher level are 'hyper-parameters' such as the level of noise; at the lower level are the physical parameters of interest (i.e. β)

that represent uplift history. For details, see Bodin et al. (2012a, 2012b).

We use a reversible jump Markov Chain Monte Carlo (rj-MCMC) algorithm (Green, 1995; Sisson, 2005) to calculate $p(\beta|\alpha)$, which treats the numbers of nodes and therefore model complexity as a free parameter. In the last decade, the reversible jump algorithm has become popular in earth sciences and has been applied to a wide range of areas, such as inversion of DC resistivity sounding data (Malinverno, 2002), geostatistics (Stephenson et al., 2004), geochronology (Jasra et al., 2006), thermochronology (Gallagher, 2012; Fox et al., 2015), climate variability (Hopcroft et al., 2009), modeling of stratigraphy (Charvin et al., 2009), geoacoustic inversion (Dettmer et al., 2010), inversion of seismic data (Piana Agostinetti and Malinverno, 2010; Bodin et al., 2013; Young et al., 2013), inversion of electromagnetic data (Ray and Key, 2012), and plate kinematic reconstruction (Iaffaldano et al., 2013). This approach is only described briefly here (see (Gallagher et al., 2009; Gallagher et al., 2011; Sambridge et al., 2013), for reviews).

The rj-MCMC algorithm is initialized with a series of random parameter values that describe $u^*(t^*)$. At each step of the walk, a new value of a model parameter is proposed based on a perturbation from the current model. The value of the proposed parameter is drawn from a Gaussian distribution centered on the current model with a standard deviation to be defined by the user. The proposed model is accepted or rejected based on an acceptance criterion. This acceptance criterion is the ratio of the probabilities of the current and proposed model. The standard deviation of the proposal distribution controls the rate at which the algorithm explores parameter space: if the standard deviation is small, perturbations are likely to be small and so parameter space is explored slowly, however many models are likely to be accepted; conversely, if the standard deviation is large, proposals are generated that are far from the current model, and possibly in a region of low probability, therefore they have a high probability of being rejected and so relatively few proposals are accepted. Once a model is accepted, this model replaces the current model and a new model is once again generated as a perturbation of the current model. This
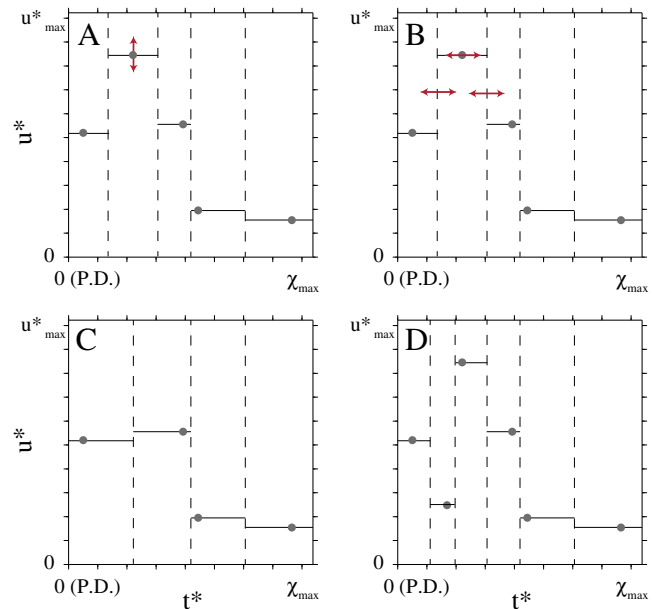
Fig. 3. Changes in $u^*(t^*)$ from proposals (1) to (4). (A) Change proposal: the value of one of the nodes can change. (B) Move proposal: the position of one of the nodes can move. (C) Death proposal: here the node highlighted in (A) has been removed. (D) Birth proposal: a new node is introduced between the first and second nodes in (A).

process typically is repeated 10,000 s of times. Accepted models are asymptotically distributed according to the target distribution in Eq. (9). They are saved and combined, and this ensemble is used to approximate the posterior probability density function.

For our problem, we have five distinct proposals that are possible: (1) the t^* value of a node can move (Move); (2) the u^* value at a node can change (Change); (3) the number of nodes describing $u^*(t^*)$ can be increased (Birth); (4) the number of nodes describing $u^*(t^*)$ can be decreased (Death); and (5) the value of σ defining data noise can also change (Noise). Proposals (1–4) are highlighted in Fig. 3. The proposed perturbations are drawn from Gaussian distributions centered on the current model with specified standard deviations of θ_1 through to θ_5 for proposals (1) to (5).

Proposals are accepted based on an acceptance probability. For Move, Change, and Noise proposals [i.e., (1), (2), and (5)] the acceptance probability is proportional to the likelihood ratio of the proposed and the current models. This approach ensures that proposals that improve data fit are always accepted, while those that decrease it are accepted with probability equal to the ratios of the likelihoods. For Birth and Death proposals [i.e., (3) and (4)], the acceptance criteria favor models that reduce data misfit, yet penalize models that are overly complex. This penalty is inflicted because although increasing the number of model parameters generally leads to a better fit to the data, it also changes the ratio of the prior probabilities for the current and proposed models. In particular, the introduction of an additional parameter leads to a much larger volume over which the prior is distributed. For a detailed description of the algorithm, we refer the reader to Bodin et al. (2012a).

MacKay (2003) showed that the magnitude of perturbations does not affect the solution but rather the sampling efficiency of the algorithm. Thus the standard deviations (θ_1 through θ_5) of the Gaussian proposal functions need to be tuned by trial-and-error in order to have an acceptance rate as close to 44% for each type of perturbation (Rosenthal, 2000).

The transdimensional posterior distribution is defined in a $2 * k$ parameter space, where k is the number of nodes, and thus, is challenging to interpret. Therefore, we project the posterior distribution into a different space and simply show a density plot of sampled rock uplift histories $u^*(t^*)$. To obtain a 'solution' for interpretation, we can simply average all the sampled models $u^*(t^*)$, by taking the mean of the distribution of u^* at each t^* or take a model which passes through the maximum of the posterior distribution.

4. Validation study: Inyo Mountains, CA, USA

In this section, we start with a validation of our method using a previously studied example from a tilted block in the Basin and Range province. We choose the Inyo Mountains because the river profiles have been extensively analyzed using the same underlying assumptions that we adopt, except that the inverse problem was tackled using a linear approach (Goren et al., 2014). Therefore, we can use the Inyo Mountains to compare our inversion approach against results obtained using a linear approach.

The Inyo Mountains are a NNW–SSE trending mountain range, with relief of almost 3 km, along the western boundary of the Basin and Range province in California (Fig. 4). The Inyo range is the first uplifted block east of the Sierra Nevada and south of the White Mountains. The normal Eastern Inyo Fault (EIF) bounds the Inyo Mountains to the east and has facilitated 1.5 km of exhumation over the past 2.8 Ma (Lee et al., 2009). Furthermore, the lithology is relatively uniform across the range (Streitz and Stinson, 1974; Ross, 1976). Therefore, rivers draining the eastern flank of the Inyo Mountains, to the flat Saline Valley, provide information on the relative rock uplift rate with respect to the sedimentary fill in the Saline Valley (Goren et al., 2014).
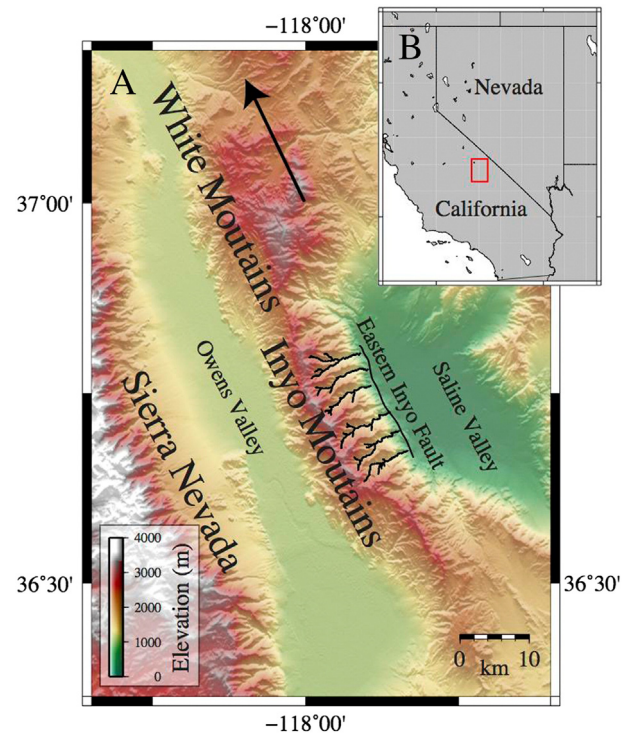

Fig. 4. Location of the Inyo Mountains, with respect to the Sierra Nevada (A) and the California–Nevada border (B). The Eastern Inyo Fault bounds the Inyo Mountains to the east and is the main structure uplifting the Inyo Mountains. The Saline Valley is an endorheic basin and defines the baselevel for rivers that drain the eastern flank of the Inyo Mountains. Rivers used in the analysis are shown as black lines. Data source: SRTM topographic data (Jarvis et al., 2006).

4.1. Inyo data set

Our dataset is composed of six drainage basins that originate at the main water divide of the Inyo Mountains and drain the eastern flank toward the EIF and the Saline Valley (Fig. 4). Elevation data were extracted from a 30 m National Elevation Dataset (NED) digital elevation model (DEM) (Gesch et al., 2002; Gesch, 2007). We extracted flow direction and upstream drainage area using the ArcGIS flow routing algorithm, and the fluvial drainage network by applying a 1-km^2 threshold for contributing area.

Fig. 5A shows the $\chi - z$ relationship for the Inyo data set, calculated with $m = 0.3$ and $A_0 = 10$ km^2, after Goren et al. (2014). The relatively well-defined trend, with only a few outlier segments, supports the assumption that these rivers shared a common rock uplift history. The $\chi - z$ relationship also shows variations in slope; and as lithology is relatively uniform in space, K is also likely to be relatively uniform in space, and thus changes in this slope are indicative of temporal variations of rock uplift rate (Perron and Royden, 2013; Royden and Perron, 2013). In the following section we present estimates of changes in the slope of this relationship obtained using a linear inverse method and the rj-MCMC algorithm presented above.

4.2. Comparison of nonlinear and linear inversion results

Goren et al. (2014) presented a linear method to infer rock uplift rates from river profiles. In their approach, the integral expression in Eq. (8) can be discretized into lengths of Δt^*, and a vector of $\mathbf{u}^*$ can be defined with an entry for each Δt^*. Therefore, the elevation of an elevation node can be described as

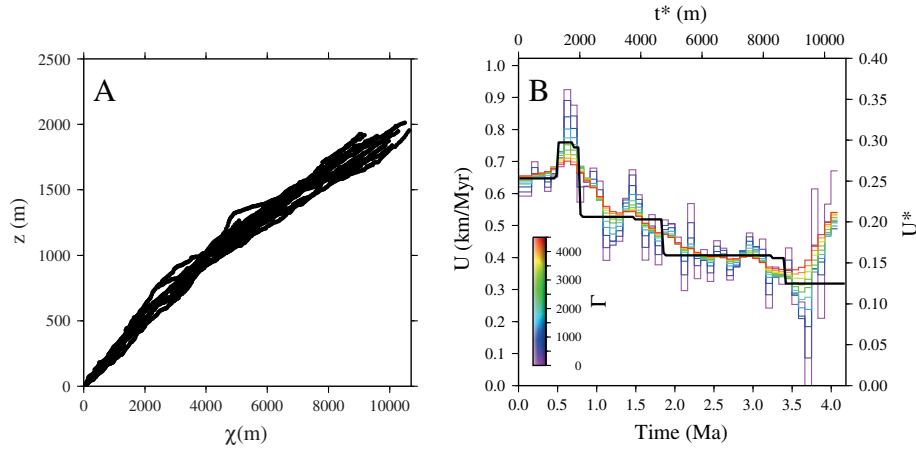$$z_i = \sum_{j=1}^{M-1} \Delta t^* u_j^* + R_i u_M^* \qquad (12)$$

Fig. 5. (A) χ–elevation relationship for rivers draining the eastern flank of the Inyo Mountains, CA. The National Elevation Dataset (NED) digital elevation model (DEM) (Gesch et al., 2002; Gesch, 2007) was used to extract the drainage network. We used $m = 0.3$ and $A_0 = 1$ km^2 to calculate χ. (B) Results of the linear inversion with the number of K-scaled time steps set to 50. Each curve shows results of a separate linear inversion with the damping parameter set to different values. The solid black curve corresponds to the maximum of the posterior distribution obtained using the rj-MCMC algorithm, shown in Fig. 6. A value of $K = 2.03 \times 10^{-5}$ m$^{0.4}$ y^{-1} was used to recalibrate u^* and t^*, after Goren et al. (2014).

where R_i is the remainder of the division $\chi_i/(M-1)$. A discrete expression for each node in the fluvial network can be defined and, as each node provides information on different portions of the same $\mathbf{u}^*$ vector, each expression can be combined as $\mathbf{Au}^* = \mathbf{z}$. Here, the matrix $\mathbf{A}$ contains blocks of scaled time, such that row$_i$ sums to χ_i. The resulting linear system of equations can be solved using a damped least squares method

$$\mathbf{u}^* = \mathbf{u}^*_{\mathbf{pr}} + \left(\mathbf{A}^{\mathbf{T}}\mathbf{A} + \Gamma\mathbf{I}\right)^{-1}\mathbf{A}^{\mathbf{T}}\left(\mathbf{Au}^*_{\mathbf{pr}} - \mathbf{z}\right) \tag{13}$$

where Γ is a damping parameter and $\mathbf{u}^*_{\mathbf{pr}}$ is the prior u^* vector used to de-trend the data, see Goren et al. (2014) for details. The damping term is used to stabilize the inverse problem, which is often ill-conditioned. Without damping, small errors in the data would propagate into very large errors in the recovered model, and the solution may be unstable and not realistic. Conversely, if the solution is overdamped, resolvable features in the χ–elevation relationship will be missed. The damping penalizes models that are far from $\mathbf{u}^*_{\mathbf{pr}}$. In this way, the solution model in Eq. (13) can be seen as a solution that minimizes two terms: (i) the least square misfit to the data; and (ii) the distance to the reference $\mathbf{u}^*_{\mathbf{pr}}$. Indeed, note that $\mathbf{u}^* = \mathbf{u}^*_{\mathbf{pr}}$ if Γ goes to infinity. Therefore Γ governs the relative contribution of these two terms.

Fig. 5B shows the results of the linear inversion with 50 time steps. Each curve represents a different result with a different value for the dampening parameter, Γ. These results show similar characteristics, although the magnitudes and timings of changes of u^* inferred for different values of Γ are quite different. Note that data noise cannot be propagated into model uncertainties in such a regularized (damped) inversion procedure, and there are no uncertainty estimates associated with the solutions. Goren et al. (2014) determined a value for the erosional efficiency of $K = 2.03 \times 10^{-5}$ m$^{0.4}$ y^{-1}, using thermochronometric data that record 1.5 km over the last 2.8 My. We also use this value of K to calibrate our results.

Next, we applied the rj-MCMC algorithm to the same data set. The algorithm was implemented on 64 parallel cpus to generate independent rj-MCMC chains, starting at different random points, and sampling the model space simultaneously and independently. We ran 10^6 models on each cpu, and tuned the values defining the proposal probabilities so that acceptance rates for proposals (1)–(5) are between 25 and 45%. The first 10,000 models form the 'burn in' phase, after which the Markov chain is thought to have converged. These first models are discarded from the posterior distribution as they are very sensitive to the initial

model, which is chosen at random. The posterior ensemble is the combination of accepted models from each cpu. Fig. 6A shows the results of the rj-MCMC algorithm for the same data set. Here the colors relate to the posterior probability of $u^*(t^*)$ and the range of u^* shows the prior values. The black and gray lines show the maximum of the posterior distribution and the expected model (respectively), which is a weighted average of the full posterior distribution. These models are useful ways to characterize the full posterior distribution.

In addition, we can calculate the probability of a change in u^* at any point in t^* (Fig. 6B). As in the linear example, we set the erosional efficiency $K = 2.03 \times 10^{-5}$ m$^{0.4}$ y^{-1} after (Goren et al., 2014) to rescale
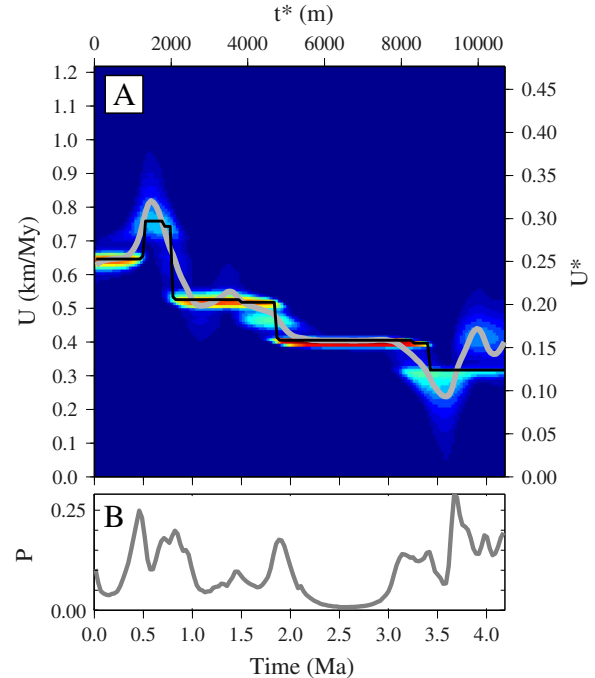

Fig. 6. (A) Posterior density distribution describing $u^*(t^*)$ for the Inyo Mountains, CA. The colors describe the relative posterior probability: red = more probable, blue = less probable. Distinct phases of constant rock uplift rate are resolved. The black line shows the maximum of the posterior distribution and the gray line is the expected model. (B) Posterior probability of a change in u^* as a function of t^*. Using a value of $K = 2.03 \times 10^{-5}$ m$^{0.4}$ y^{-1} Goren et al. (2014) calibrates u^* and t^*. (For interpretation of the references to color in this figure legend, the reader is referred to the web version of this article.)
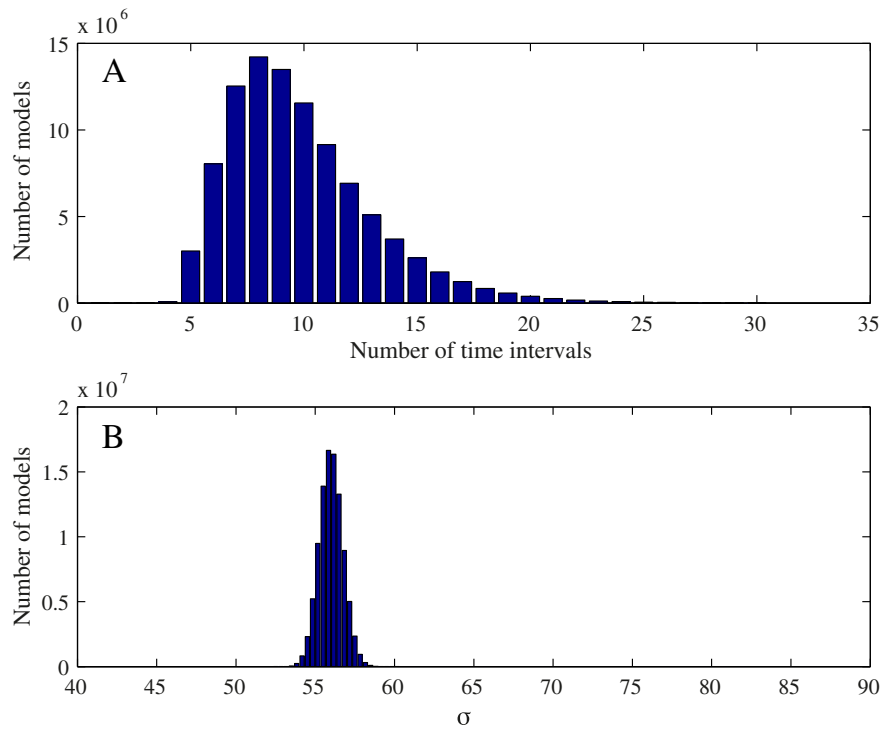
Fig. 7. (A) Histogram of the number of distinct phases of rock uplift rate for each model in the posterior distribution for the Inyo Mountains, CA. (B) Histogram, or posterior probability distribution, of σ representing geomorphic noise. The number of models in the posterior distribution is proportional to the probability.

the rock uplift rate history. Finally, we can extract estimates of the number of phases of rock uplift rate (Fig. 7) and the σ value, representing geomorphic noise (Fig. 7).

Results obtained using the fully nonlinear inversion scheme (Fig. 6B) show similar results to results obtained using the linear inversion scheme (Fig. 5B) with carefully chosen damping parameters and time step lengths. The similarity between these two solutions validates our inversion approach. In both cases, from 4 to 3 Ma, the relative uplift rate is roughly constant at about 0.4 mm/y, then from 3 Ma to ~1 Ma it increases gradually to a value of 0.55 mm/y. This is followed by a faster increase to a value of ~0.68 mm/y at about 1 Ma, which then stays roughly constant until the present. The advantages of our nonlinear approach are described below. First, user-defined damping parameters are not required and thus the nonlinear inversion scheme is more robust. Second, we are able to quantify the full state of knowledge of the model parameters. For example, between ~1.5 Ma and 2 Ma the posterior distribution displays 3 peaks with almost equal probability. Third, we predict the probability of identifying a fluvial knickpoint at specific χ values within the landscape. In the case of a damped linear inversion, knickpoints may be obscured by imposed smoothness or noise in the data set. This is observed in Fig. 5B where robust trends are more easily recognizable in the highly damped solutions; however, discrete jumps in rock uplift rate are less well recovered. In contrast, with little damping, we predict chaotic jumps in rock uplift rate that are not representative of reality. Furthermore, the exact χ value of a knickpoint may be incorrectly identified, as it would be required to be a multiple of the timestep length. The disadvantage of our approach is that many models are required to approximate the posterior distribution, thereby increasing computational time. In this example, the linear inverse solution takes approximately a second, while the nonlinear scheme takes several hours. This comparison demonstrates that our inversion approach is able to recover the correct rock uplift rate history (under the assumptions of block rock uplift, constant K in space and time, and that erosion can be parameterized using a detachment-limited linear stream power model) along with an estimate of when changes in rock uplift rate are required by the topography.

5. Southwest Peru χ data set

Having demonstrated the applicability of our method, we now apply it to the Cotahuasi–Ocoña catchment in Peru using the ^{4}He/^{3}He thermochronometric data from Schildgen et al. (2010). We extracted the drainage network for the Cotahuasi–Ocoña catchment from the global hydrological database (Lehner et al., 2008), which has a resolution of ~90 m. We calculated χ values for all pixels with an upstream drainage area >1 km^2, using $A_0 = 1$ m^2. A value of m was estimated following a trial and error approach, in which we systematically varied m and inspected elevation scatter after Willett et al. (2014). We found that a value of $m = 0.35$ resulted in little elevation scatter with clear tends in the χ–elevation relationship that are indicative of river capture. In addition, we expect that values of m and K will covary (e.g. Berlin and Anderson, 2007; Croissant and Braun, 2014) such that if we select a different value of m, a different value of K will be determined during the calibration phase, although the inferred rock uplift history would be similar. Therefore we do not expect the exact value of m to be a primary source of uncertainty in the analysis. However, as the elevation scatter is sensitive to m, using a different value of m will likely lead to a different inferred value of geomorphic noise.

The resulting map of χ values shows that numerous small-scale drainage divides at relatively low elevations appear to be migrating (Fig. 8A), where different values of χ are identified on different sides of drainage divides (Shelef and Hilley, 2014; Willett et al., 2014). We assume that these small-scale effects will have a negligible effect on our conclusions. However, larger-scale drainage basin reorganization is also observed in the upper reaches of the Cotahuasi–Ocoña catchment and can be identified from the map of χ by the differences in χ values across divides (Fig. 8B).

We expect that the process of drainage basin reorganization will have an appreciable effect on the inferred rock uplift history (Willett et al., 2014). To assess this effect, we show χ values as a function of elevation (Fig. 8C). Here we have reduced the number of pixels in the drainage network from 31,778 by a factor of 10, to increase the clarity of the figure, but note that we use the full data set for the analysis
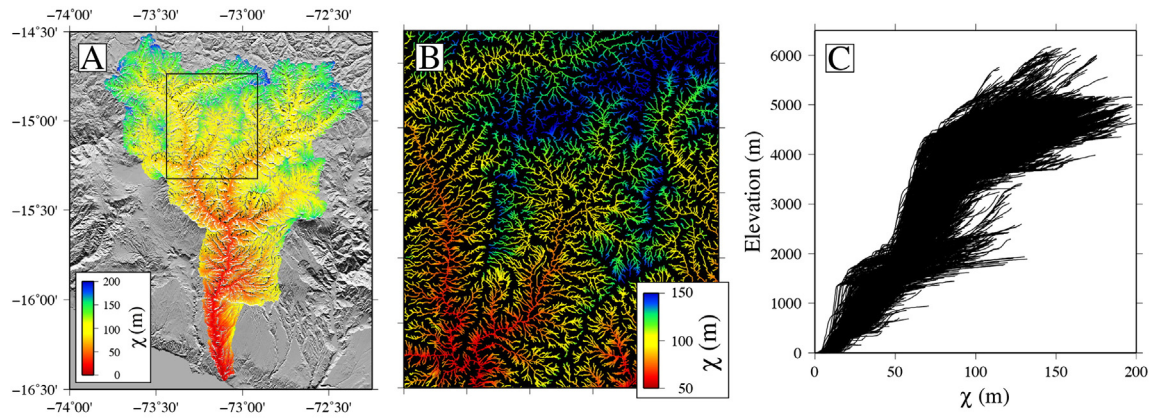
Fig. 8. (A) χ values for the Cotahuasi–Ocoña Canyon and tributaries. We use a value of $m = 0.35$ and $A_0 = 1$ m^2 to calculate χ. (B) χ values highlighted for the black box in (A). Here the drainage basin at the center of the panel appears to be losing drainage area as the χ values at the drainage divides are larger than the neighboring basins. (C) χ–elevation relationship for the drainage network shown in (A). Considerable scatter in the data masks obvious trends.

presented below. We observe an increase in χ as a function of elevation with a close to linear increase with elevation up to ~4000 m and a χ value of ~100 m. We observe considerable scatter in this χ–elevation relationship, which makes identifying robust trends challenging. In the subsequent section we extract the posterior probability $u^*(t^*)$ along with a term describing this scatter reflecting geomorphic noise.

6. Results and discussion

We applied the rjMCMC algorithm to the χ–elevation data set for the Cotahuasi–Ocoña catchment. As in the Inyo Mountains example, we tuned the values defining the proposal probabilities so that acceptance rates are between 25 and 45% and discarded models from the 'burn in' phase.
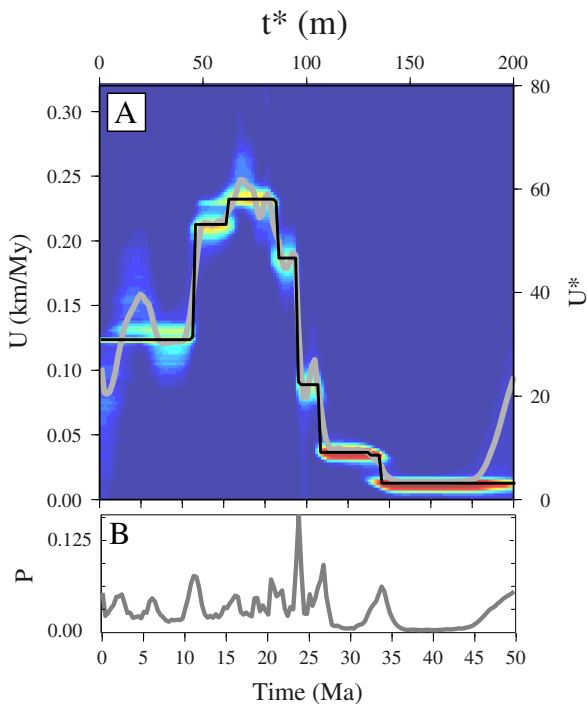

Fig. 9. (A) Posterior density distribution describing $u^*(t^*)$ for the Cotahuasi–Ocoña catchment χ–elevation data. The colors describe the relative posterior probability: red = more probable, blue = less probable. (B) Posterior probability of a change in u^* as a function of t^*. $K = 4$ m$^{0.3}$ My^{-1} is used to calibrate the results after comparison with measured cooling history (Schildgen et al., 2010) shown in Fig. 12. (For interpretation of the references to color in this figure legend, the reader is referred to the web version of this article.)

Results highlight a complex u^* function with variable uncertainty through t^* (Fig. 9A). The solid black line shows the expected model, which is the weighted average of the posterior probability and is effectively the mean solution. Fig. 9B shows the relative probability that changes in u^* occurred at specific values of t^*. We identify at least four distinct changes of u^*. Several other changes in u^* may also be identified, but these are associated with lower probabilities and are less reliable. In general, we observe that where the scatter in the χ–elevation relationship is larger, we predict larger uncertainty in the u^* function.

The misfit between the measured and predicted elevations for the inferred $u^*(t^*)$ function can be compared using two approaches. We predict elevations using a model of $u^*(t^*)$ that passes through the maximum of the posterior distribution and Eq. (8). First, we plot model residuals as a function of space. These residuals indicate whether the errors are randomly distributed or whether there are systematic residuals indicating that our model fails to capture certain complexities. Although many of the residuals are small and randomly distributed, we also observe areas with large, systematic residuals (Fig. 10A). In particular, the basin in the upper reaches of the Cotahuasi–Ocoña catchment — that we identified as actively loosing drainage area — shows systematic positive residuals. This indicates that this catchment is not incising at the same rate as the surrounding basins and thus plots higher on the χ–elevation relationship. Another region of large residuals is shown in the eastern region of the analysis. Here multiple volcanoes rise out of the relatively flat plateau. These volcanoes are short wavelength features that do not reflect rock uplift, and our model poorly reproduces their elevations. We also observe large residuals at ~−16°S that may be related to a combination of drainage divide migration, and short wavelength uplift associated with active structures that are observed farther to the south (Schlunegger et al., 2006).

To further investigate the misfit between the measured and predicted elevations for the inferred $u^*(t^*)$ function, we show the predicted elevation data as a function of measured elevation (Fig. 10B). Departures from the 1:1 line highlight where the observed data are poorly matched by the predicted data. In general, the correlation between the observed data and the predicted data is good for all elevations, and the r^2 value is equal to 0.89. This highlights that the simple block uplift model we assume can explain ~90% of the observed data.

In order to calibrate our results to an absolute time scale, we use apatite ^{4}He/^{3}He thermochronometric data from the Cotahuasi–Ocoña catchment (Schildgen et al., 2010). In Fig. 12, we show a randomly generated set of time–temperature paths that fit the ^{4}He/^{3}He data, after Schildgen et al. (2010). Since the ^{4}He/^{3}He data constrain the path and rate of cooling through ~80–30 °C (Shuster and Farley, 2004), they constrain the timing of 2–3 km of canyon incision. These data
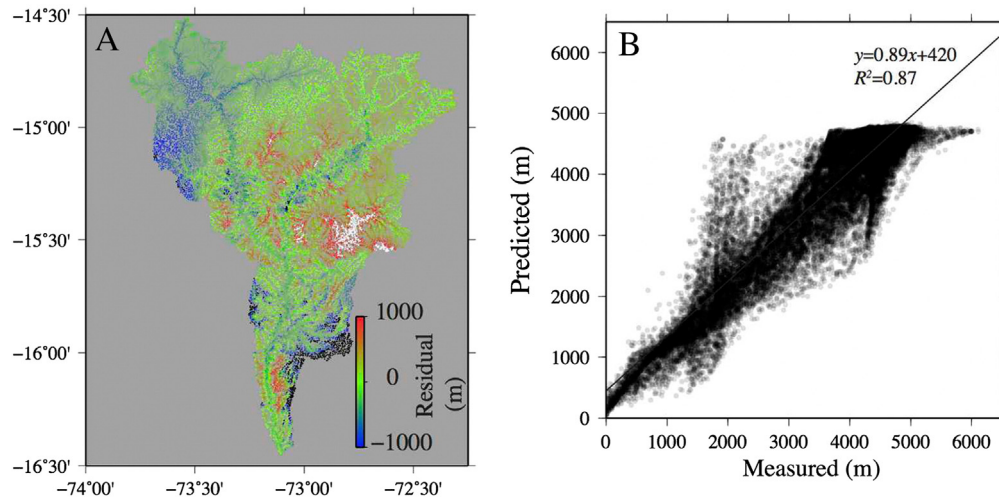
Fig. 10. (A) Map of residuals for the maximum of the posterior distribution. (B) Model-predicted elevation as a function of observed elevation. The predicted elevations agree reasonably well with the observed data, indicated by the high R^2 value.

indicate that bedrock now exposed at the base of the middle portion of the canyon cooled rapidly from 10 to 3 Ma. Therefore, we use these data to calibrate our model by calculating an incision history for the canyon using our uplift function that passes through the maximum of the posterior distribution and Eq. (8). In order to use this integral expression to calculate topography at a different t^* value, we shift the integral bounds by the relevant amount (Goren et al., 2014). We then calculate K-scaled erosion rate using the stream power model through the t^* history (Fig. 11). In turn, we extract K-scaled erosion rate history for the same portion of the canyon as where ^{4}He/^{3}He thermochronometric data have been obtained. Based on the low measured surface heat flux of 30 to 60 mW/m^2 for the inland regions of the forearc (Springer, 1999), we assume a geothermal gradient of 20°/km to compare the exhumation history we infer with the cooling paths. By using a range of K values, we can adjust the erosion rate history to match the cooling history constrained by the data. We find that a K value of 4 m$^{0.3}$ My^{-1} provides a reasonable fit to the cooling history (see Fig. 12).

Using this calibrated K value, we are able to rescale u^* and t^* to u and t (Fig. 9A). Our results suggest that the onset of rock uplift of the central

Andean Plateau occurred at ~25 Ma, almost 10 Ma y earlier than the observed increase in the rate of canyon incision (Schildgen et al., 2010). Several later episodes of rock uplift are inferred with a rapid increase in rock uplift rate at ~25 Ma. Rates of rock uplift range between close to 0 mm/y, during the earliest part of the rock uplift history constrained by the river profiles, to ~0.25 mm/y over the time interval 20 to 10 Ma. A decrease in rock uplift rate is also resolved at ~10 Ma. This recent decrease also leads to a decrease in erosion rate over the last 2 Ma within the canyon, which is consistent with ^{40}Ar/^{39}Ar ages of 2.261 ± 0.046 Ma for a basaltic andesite flow sampled 125 m above the present valley floor (Schildgen et al., 2007). Farther upvalley, an ignimbrite (05TS25) perched ~400 m above the present valley shows that ~75% of the canyon depth (1.6 km total local incision) was cut before 3.825 ± 0.016 Ma. However, we overpredict the amount of incision over the last 2 Ma, and this is discussed below.

Jeffery et al. (2013) analyzed the form of the trunk channel of the Cotahuasi–Ocoña catchment, along with incision constraints, to derive a rock uplift rate history and infer key parameters controlling fluvial incision. In their analysis, they adopted an alternative forward model
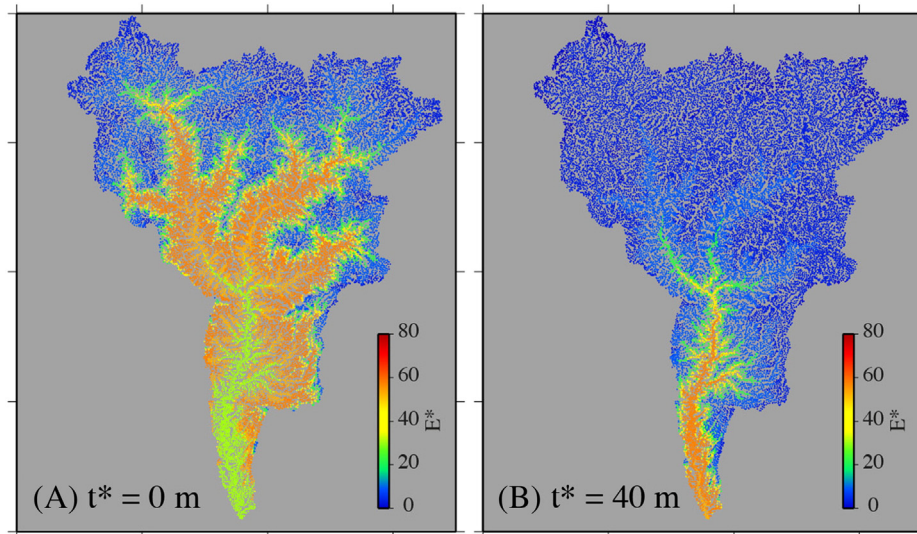

Fig. 11. K-scaled erosion rate for predicted topography using the maximum posterior model at $t^* = 40$ m (B) and the present day, $t^* = 0$ m, (A). If $K = 4$ m$^{0.3}$ My^{-1} these t^* values correspond to 0 and 10 Ma and the erosion rate color scale varies from 0 to 0.32 km/My. At $t^* = 40$ m (B), K-scaled erosion rate is low across much of the catchment. A fluvial knickpoint separates the region of low K-scaled erosion rate from the lower reaches of the canyon. By the present day (A), low K-scaled erosion rate is predicted for the highest reaches. A band of high K-scaled erosion rate is predicted at intermediate elevations. In addition, low K-scaled erosion rate is predicted at lower elevations.
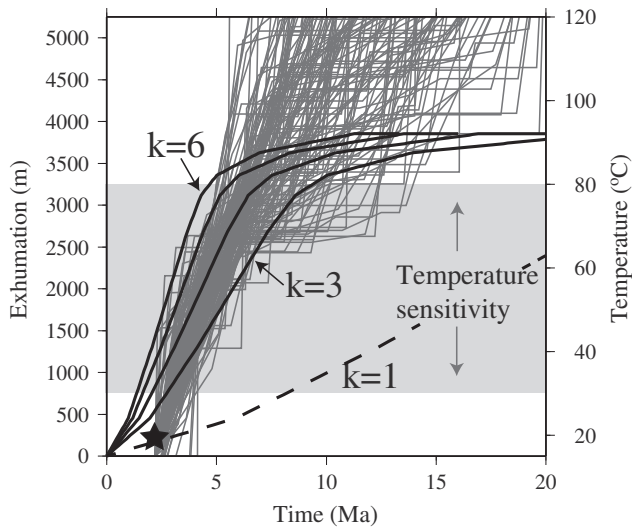
Fig. 12. Predicted *K*-scaled exhumation history for the location shown in Fig. 1B. Systematically varying the erodibility, *K*, allows us to rescale the exhumation history to match the representative cooling history derived by Schildgen et al. (2010). We have used a geothermal gradient of 20 °C/km to compare exhumation and temperature. As we have calibrated $u^*(t^*)$ based on the timing of incision and not the rate, our results are not sensitive to changes in the geothermal gradient. Five *K* values are shown, 1, 3, 4, 5, and 6 m$^{0.3}$ My^{-1}, black curves, using the maximum posterior probability solution from Fig. 9. We find that a value $K = 4$ m$^{0.65}$ My^{-1} provides the closest agreement between the predicted exhumation history and the cooling history.

Fig. 13. Independent estimates of paleoelevation highlighting the pulsed surface uplift of the Andean Plateau. Constraints obtained from oxygen isotopes of precipitation (Garzione et al., 2006), leaf physiognomy (Gregory-Wodzicki, 2002), Δ47 paleothermometry (Ghosh et al., 2006; Garzione et al., 2014), and δD paleothermometry (Saylor and Horton, 2014), modified after Garzione et al. (2014). Black curves show surface uplift histories for the same erodibility values as shown in Fig. 12, using the maximum posterior probability solution from Fig. 9.

to simulate fluvial incision that incorporated the effects of channel width and threshold incision rate. Furthermore, precipitation was assumed to increase through time owing to the orographic effect of plateau uplift based on simulated changes in regional climate (Insel et al., 2010; Poulsen et al., 2010). Using a Monte Carlo approach in which the complexity (i.e., number of phases of rock uplift) of the model was specified a priori, different rock uplift rate histories and fluvial incision parameters were investigated. Importantly, the magnitude of the rates of rock uplift, and the decrease in rates at 10 Ma, presented here are consistent with the results of Jeffery et al. (2013), despite the linear stream power model we adopt. The rock uplift rate we present in Fig. 9A, however, appears to be more punctuated. One explanation for this is that the results of our inversion of the χ–elevation data have been rescaled to a rock uplift history using a single value of *K*. In fact, different values of *K* will lead to different rock uplift rate histories, and some of these will be less punctuated. Therefore, we convey the additional surface uplift histories for different values of *K* that fit the cooling histories inferred from the ^{4}He/^{3}He in the subsequent section.

6.1. Independent constraints and additional complexities

Independent estimates of surface uplift provide a means to validate our results and test the underlying assumptions. Paleoelevation estimates have been made across much of the Altiplano, and these are summarized in Fig. 13. These constraints, from a wide range of techniques, suggest a rapid pulse of 2 km of surface uplift occurred between 16 and 13 Ma in the southern Altiplano and ~7 My later to the north (Gregory-Wodzicki, 2002; Garzione et al., 2006, 2014; Ghosh et al., 2006). In addition, Picard et al. (2008) used molecular phylogenetics of highland biotaxa to estimate that the plateau had reached heights of 2.0–2.5 km by the middle to late Miocene. However, estimates of paleoatmospheric temperatures from hydrogen isotope analysis (δD) in volcanic glass from Miocene deposits found <200 km east of the Cotahuasi–Ocoña catchment, suggest that this part of the plateau had reached its current elevation by 16 Ma (Saylor and Horton, 2014). These differences indicate that the surface uplift history may be more
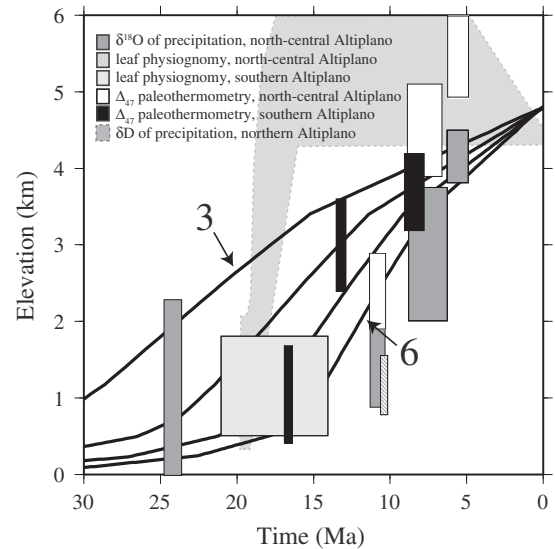
complex than previously thought (Saylor and Horton, 2014). To compare our inferred rock uplift rate history with independent estimates of surface uplift, we calculate topography through time and track the highest calculated elevation point. The inferred surface uplift rate histories for $K = 3$, 4, 5, and 6 m$^{0.3}$ My^{-1} are shown in Fig. 13 and are predictably different for each *K* value.

The history of surface uplift that we constrain agrees reasonably well with the overall trend of surface uplift determined from independent constraints (Fig. 13). Interestingly, our results for the preferred *K* value of 4 m$^{0.3}$ My^{-1} are more consistent with the surface uplift record of the southern Altiplano than the central Altiplano. The internal consistency of these independent data sets builds confidence in the underlying assumptions of our analysis. However, the rate of surface uplift during the uplift pulse (i.e. from 20 to 10 Ma) quantified from our river profile analysis appears to be less than the rate inferred from the stable isotope and leaf physiognomy paleoelevation studies (Fig. 13). In the following two sections, we discuss two complexities in our analysis, which may lead to an underestimation of the rock uplift rate during this pulse.

6.2. Influence of climate change

It has been proposed that the regional climate became increasingly arid through the Miocene (Hartley, 2003; Schlunegger et al., 2010; Pingel et al., 2014) because of the rain shadow produced by uplift of the Andean Plateau. Alternatively, it has been proposed that uplift of the Andean Plateau has led to increased precipitation across the Andean Plateau (Insel et al., 2010; Poulsen et al., 2010), which leads to higher precipitation in the headwaters of the Cotahuasi–Ocoña catchment (Jeffery et al., 2013). Thus our assumption of uniform *K* through time may be invalid. If the climate did change, the inferred rock uplift rate would be overestimated for some parts of the history and underestimated for other parts, and this distortion will depend on (i) the function of the climate change leading to a change in *K*, and (ii) the time interval over which we use independent measures of rock uplift rate or incision to calibrate the results. We highlight these effects with a simplified synthetic example designed to resemble the inferred rock uplift rate and possible climatic scenarios in the
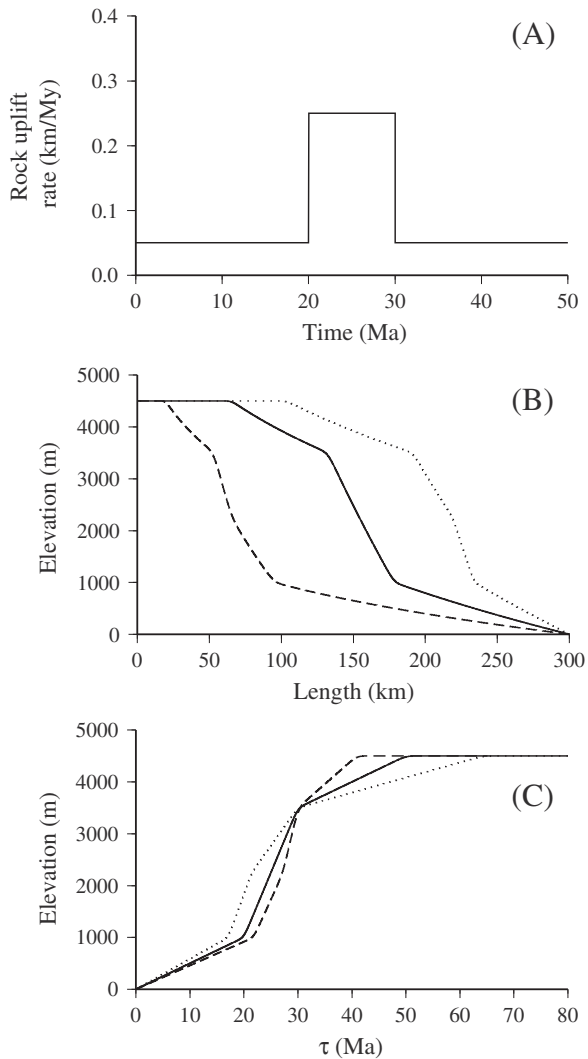
Fig. 14. Influence of climate change on inferred rock uplift history. (A) Rock uplift history used to produce the synthetic data designed to resemble the inferred history for the Cotahuasi–Ocoña Canyon. Climate change is parameterized by varying K through time for three different climatic scenarios: (1) constant K through time of 2 m$^{0.2}$ My^{-1}; (2) decrease in K to 1 m$^{0.2}$ My^{-1} at 25 Ma; (3) increase in K to 4 m$^{0.2}$ My^{-1} at 25 Ma. (B) Predicted river profiles for the rock uplift rate history shown in (A) using the three climatic scenarios, black line = scenario 1, dotted line = scenario 2, dashed line = scenario 3. (C) Calculated τ–elevation relationships for the three scenarios using a synthetic thermochronometric constraint of 3500 m since 30 Ma to determine an average K value and calibrate the results. With respect to scenario 1, the τ–elevation relationships for different segments are under- or overestimated, which results in a distorted rock uplift rate history.

Cotahuasi–Ocoña catchment. A 300-km-long river profile was modeled using the rock uplift rate history shown in Fig. 14A. We used Hack's law,

$$L = 1.6A^{0.6} \tag{14}$$

where L is channel length and A upstream drainage area (Hack, 1973) to assign values of upstream drainage area along the length of the river. The exponents in the stream power model were $m = 0.4$ and $n = 1$. The stream power model was solved using an implicit finite difference method (Braun and Willett, 2013) with time steps of 0.01 My and grid nodes every 300 m along the length of the river. We modeled three different climatic scenarios by changing the value of the erosional efficiency, K, through time (Fig. 14A): (i) K is set to 2 m$^{0.2}$ My^{-1} for the entire history; (ii) K decreases at 25 My into

the simulated rock uplift history to 1 m$^{0.2}$ My^{-1} to reflect a decrease in erodibility or an increase in aridity; (iii) K increases at 25 My into the simulated rock uplift history to 4 m$^{0.2}$ My^{-1} to reflect an increase in erodibility.

Fig. 14B shows the simulated longitudinal profiles of the rivers for the three geomorphic scenarios. All profiles show four distinct segments that represent (from the top of the profile downstream) the relict landscape prior to any uplift, the initial low uplift rate, the pulse of high uplift rate, and the return to low rock uplift rate. In the second climatic scenario in which K decreases at 25 My, dotted profile, the knickpoints separating these segments are all shifted downstream compared to the reference model. Conversely, in the third climatic scenario, dashed line, knickpoints are located farther upstream as the increase in K leads to an increased rate of knickpoint retreat. In turn, these profiles have dramatically, yet predictably, different χ–elevation relationships, and therefore the u^* history we infer would be very different. However, the inferred values of K would also be very different.

To calibrate the results, we assume that thermochronometric data exist that record the correct amount of incision associated with the pulse of rock uplift rate at the correct time. These data could come from close to the base level of the river and would record exhumation over the last 30 Ma. Using these synthetic data we convert χ to τ (Fig. 14C) and the slope of this relationship provides an estimate of the rock uplift rate. For the first climatic scenario, the slope of the τ–elevation relationship provides the reference rock uplift rate history, which was used to produce this relationship. For the second climatic scenario, the τ–elevation relationship overestimates the rock uplift rate during the recent history and part of the pulse until ~25 Ma, which is the time of change in K, when the slope decreases with respect to the reference model. In contrast, the third climatic scenario leads to an opposite effect. All rock uplift histories are forced to pass through the constraint provided by the thermochronometric data of ~3500 m of rock uplift over the last 30 Ma. In reality, the potential to under- or overestimate portions of the rock uplift rate history would be a function of complicated variations of K through time and a function of the time over which rock uplift rate has been constrained.

We observe features in our results that support a decrease in K through time, indicative of a change in climate, during or after surface uplift of the Andean Plateau. In particular, our results do not capture the very low, recent erosion rates that are constrained by the basaltic andesite flow found 125 m above the present valley floor (Schildgen et al., 2007). Indeed, if this constraint alone was used to calibrate our results, a K value of ~1 m$^{0.4}$ My^{-1} would be inferred (dashed line Fig. 12). However, as we have used the thermochronometric data that constrain erosion rate over a longer period of time, the general features of our inferred uplift history are robust as shown by the synthetic example. In future studies, erosion rate constraints through time may provide the leverage to infer a continuous record of how K varies through time, by identifying changes in erosion rate without the corresponding changes in the τ–elevation relationship.

6.3. Linearity of the stream power model

An alternative explanation of the slow recent erosion rates may be related to a failure of the linear stream power model to adequately describe the evolution of the catchment. Two possible complexities to the stream power model may lead us to underestimate the rock uplift rate during the pulse. First, a sediment flux dependence on the river incision has been proposed in several settings (Sklar and Dietrich, 1998; Whipple and Tucker, 2002; Wobus et al., 2006; Lamb et al., 2008; Lague, 2010; Yanites et al., 2011). This would lead to a degradation of steep channel segments through time, therefore an abrupt pulse of rock uplift rate would appear as a smoother feature in our results, and the magnitude of the pulse would be underestimated. In addition, a transition to a transport-limited system may be expected

following a decrease in rock uplift rate; and this could potentially explain the low erosion rates averaged over the last 2 Ma, as proposed by Jeffery et al. (2013). Second, if the exponent on the slope of the stream power model, n, is greater than one, as has been suggested (Kirby and Whipple, 2001; Attal et al., 2008), the magnitude of the pulse of rock uplift rate would also be underestimated, as shown by Goren et al. (2014). As above, incorporating geological constraints may provide the leverage to infer erosional parameters, as has been investigated by Jeffery et al. (2013). Therefore, incorporating geological data into our analysis in the future may provide redundant information that can be exploited to further our understanding of fluvial erosion.

6.4. Spatial variations in rock uplift rate and precipitation

We have assumed that the rock uplift rate and precipitation are both spatially uniform; in this section we investigate implications of that assumption. Evidence exists for active growth of a large-scale (>20 km) anticline within the forearc to the south of our study site (Schlunegger et al., 2006). If a band of high rock uplift caused by anticline growth influenced the Cotahuasi–Ocoña catchment, a corresponding band of steepened rivers would be expected, forming a stationary knickzone. Our analysis would mistake such a band of steepened rivers for a transient signal resulting from a pulse of rock uplift. However, we do not interpret our inferred pulse in rock uplift as owing to such anticline development because we see no evidence for this large-scale structure in the vicinity of the Cotahuasi–Ocoña catchment. There is evidence for small-scale faulting within the forearc in this region; however, there is only ~100 m of vertical movement across the largest fault since ~16 Ma (Roperch et al., 2006; Schildgen et al., 2009). Finally, the presence of a regional paleosurface attests to significant regional tilting since 16 Ma, and tilted forearc deposits in northern Chile provide evidence of 1 to 2 km of differential uplift of the plateau margin relative to the coast after 11 to 10 Ma (Schildgen et al., 2007; Jordan et al., 2010). If lower rock uplift rates are found at the southern margin of the catchment and the channel is incising in response to this tilting, the channel steepness would be expected to increase toward the north. Under the assumption of spatially invariant rock uplift rate, we would thus infer a decrease in rock uplift rate through time as the dominant trend in χ values is increasing toward the north. Importantly, this tilting would not lead us to infer a pulse of rock uplift.

Measured modern precipitation is not spatially uniform; along the western flank of the central Andes at 15 to 17°S precipitation ranges from 8 mm/y at the coast to 1000 mm/y at 4500 m elevation (Houston and Hartley, 2003; Steffen et al., 2010). The main effect of this differential precipitation is that the relationship between drainage area and discharge will break down and thus A^m will poorly approximate discharge. However, as the main channel runs roughly perpendicular to the gradient of precipitation, changing the value of m, we can account for the first-order effects of spatial variations in precipitation. This is a potential explanation for why we inferred a value of $m = 0.35$, as opposed to the canonical value of $m = 0.5$: using $m = 0.35$ decreases the rate at which A^m approaches 0, effectively providing higher discharge in the headwaters relative to the trunk channel. However, in the southern part of the catchment, the main trunk will have a higher discharge than the tributaries, compared to what would be expected based on the upstream drainage area. Therefore, tributaries in the south will become steeper than expected. We note that these southern tributaries are associated with systematic residuals. It is unclear whether these residuals are the result of spatial variations in precipitation or drainage divide migration. We do not explore this differential precipitation further because of uncertainty associated with projecting this spatial pattern of precipitation back through time. Further work is required to account for spatial variations in rock uplift or precipitation within our inverse framework, and this may explain more of the scatter in the χ–elevation relationship.

7. Conclusion

We have developed a new approach to investigate rock uplift histories from fluvial drainage networks. We use a fully nonlinear Bayesian approach to describe posterior probability of $u^*(t^*)$ along with the probability of changes in u^* at a specific value of (t^*). In addition, our approach enables us to quantify geomorphic noise, which may be associated with a large range of processes. In this respect, our approach enables us to distinguish between changes in rock uplift and small-scale features of the topography, with respect to the total elevation change. Interrogating the residuals would enable the processes responsible for landscape evolution to be revealed with increased clarity. However, it is important to note that a large percentage of the topography of the Cotahuasi–Ocoña catchment can be explained with a relatively simple uplift history.

The inversion approach utilized here enables us to overcome a number of well-known issues associated with standard inversion schemes. First, the Bayesian inference approach provides a stable solution with no need for explicit regularization; that is, no user-supplied damping term nor tuning of trade-off parameters are required. Second, the procedure involves a dynamic parametrization for the model that is able to consider the variability of the information provided by data. The output is an ensemble of models for uplift history that are distributed according to a posterior probability distribution. Meaningful statistical information can be extracted from this ensemble of models. Uncertainty estimates can also be inferred, which better capture the variability in the range of possible solutions than a single (e.g. best) model. However, a limitation of this approach over the linear inversion approach is that many forward models need to be run.

We have inferred a rock uplift history for the north-central Andean Plateau from the Cotahuasi–Ocoña catchment and available thermochronometric data. By using thermochronometric data, which record exhumation over the last 10 My, to calibrate the results enables us to 'average-out' the effects of short-term changes in K. Our calibrated rock uplift history reveals a pulse of rock uplift between 25 and 10 Ma at rates as high as 0.25 km/My. However, the rock uplift rate inferred during this pulse is not as high as is predicted if the central Andean Plateau grew as a result of loss of unstable lithospheric mantle (Houseman et al., 1981) or lower crustal flow (Husson and Sempere, 2003). Instead, our results are more consistent with models that require gradual uplift of the north-central Andean Plateau. Alternatively, the analysis of river profiles here may lead to an underestimation of the rate of rock uplift during the pulse because of unaccounted complexities, for example nonlinearity in the stream power model owing to a sediment flux control on fluvial incision or changes in regional climate. By combining independent estimates of rock uplift rate or surface uplift, these complexities can be incorporated into the model for further investigation.

References

Akaike, H., 1974. A new look at the statistical model identification. Autom. Control IEEE Trans. 19 (6), 716–723. http://dx.doi.org/10.1109/TAC.1974.1100705.

Attal, M., Tucker, G.E., Whittaker, A.C., Cowie, P.A., Roberts, G.P., 2008. Modeling fluvial incision and transient landscape evolution: influence of dynamic channel adjustment. J. Geophys. Res. Earth Surf. 113 (F3). http://dx.doi.org/10.1029/2007JF000893.

Barnes, J., Ehlers, T., 2009. End member models for Andean Plateau uplift. Earth Sci. Rev. 97 (1), 105–132. http://dx.doi.org/10.1016/j.earscirev.2009.08.003.

Berlin, M.M., Anderson, R.S., 2007. Modeling of knickpoint retreat on the Roan Plateau, western Colorado. J. Geophys. Res. Earth Surf. 112 (F3). http://dx.doi.org/10.1029/2006JF000553.

Bishop, P., Hoey, T.B., Jansen, J.D., Artza, I.L., 2005. Knickpoint recession rate and catchment area: the case of uplifted rivers in eastern Scotland. Earth Surf. Process. Landf. 30 (6), 767–778. http://dx.doi.org/10.1002/esp.1191.

Bodin, T., Sambridge, M., Tkalčić, H., Arroucau, P., Gallagher, K., Rawlinson, N., 2012 aa. Transdimensional inversion of receiver functions and surface wave dispersion. J. Geophys. Res. Solid Earth 117 (B2). http://dx.doi.org/10.1029/2011JB008560.

Bodin, T., Sambridge, M., Tkali, H., Arroucau, P., Gallagher, K., Rawlinson, N., 2012 bb. Transdimensional inversion of receiver functions and surface wave dispersion. J. Geophys. Res. Solid Earth 117 (B2). http://dx.doi.org/10.1029/2011JB008560.

Bodin, T., Yuan, H., Romanowicz, B., 2013. Inversion of receiver functions without deconvolution—application to the Indian craton. Geophys. J. Int. ggt431 http://dx.doi.org/10.1093/gji/ggt431.

Braun, J., Willett, S.D., 2013. A very efficient O (n), implicit and parallel method to solve the stream power equation governing fluvial incision and landscape evolution. Geomorphology 180, 170–179. http://dx.doi.org/10.1016/j.geomorph.2012.10.008.

Charvin, K., Gallagher, K., Hampson, G., Labourdette, R., 2009. A Bayesian approach to inverse modelling of stratigraphy, part 1: method. Basin Res. 21 (1), 5–25. http://dx.doi.org/10.1111/j.1365-2117.2008.00369.x.

Cohen, S., Willgoose, G., Hancock, G., 2008. A methodology for calculating the spatial distribution of the area–slope equation and the hypsometric integral within a catchment. J. Geophys. Res. Earth Surf. 113 (F3). http://dx.doi.org/10.1029/2007JF000820.

Croissant, T., Braun, J., 2014. Constraining the stream power law: a novel approach combining a landscape evolution model and an inversion method. Earth Surf. Dyn. 2, 155–166. http://dx.doi.org/10.5194/esurf-2-155-2014.

Davis, W.M., 1899. The geographical cycle. Geogr. J. 14 (5), 481–504. http://dx.doi.org/10.2307/1774538.

Dettmer, J., Dosso, S., Holland, C., 2010. Trans-dimensional geoacoustic inversion. J. Acoust. Soc. Am. 128, 3393. http://dx.doi.org/10.1121/1.3500674.

DiBiase, R.A., Whipple, K.X., Heimsath, A.M., Ouimet, W.B., 2010. Landscape form and millennial erosion rates in the San Gabriel Mountains, CA. Earth Planet. Sci. Lett. 289 (1), 134–144. http://dx.doi.org/10.1016/j.epsl.2009.10.036.

Flint, J.J., 1974. Stream gradient as a function of order, magnitude, and discharge. Water Resour. Res. 10 (5), 969–973. http://dx.doi.org/10.1029/WR010i005p00969.

Fox, M., Goren, L., May, D.A., Willett, S.D., 2014. Inversion of fluvial channels for paleorock uplift rates in Taiwan. J. Geophys. Res. Earth Surf. http://dx.doi.org/10.1002/2014JF003196.

Fox, M., Leith, K., Bodin, T., Balco, G., Shuster, D.L., 2015. Rate of fluvial incision in the Central Alps constrained through joint inversion of detrital ^{10}Be and thermochronometric data. Earth Planet. Sci. Lett. 411, 27–36. http://dx.doi.org/10.1016/j.epsl.2014.11.038.

Gallagher, K., 2012. Transdimensional inverse thermal history modeling for quantitative thermochronology. J. Geophys. Res. Solid Earth 117 (B2). http://dx.doi.org/10.1029/2011JB008825.

Gallagher, K., Charvin, K., Nielsen, S., Sambridge, M., Stephenson, J., 2009. Markov chain Monte Carlo (MCMC) sampling methods to determine optimal models, model resolution and model choice for Earth Science problems. Mar. Pet. Geol. 26 (4), 525–535. http://dx.doi.org/10.1016/j.marpetgeo.2009.01.003.

Gallagher, K., Bodin, T., Sambridge, M., Weiss, D., Kylander, M., Large, D., 2011. Inference of abrupt changes in noisy geochemical records using transdimensional changepoint models. Earth Planet. Sci. Lett. 311 (1), 182–194. http://dx.doi.org/10.1016/j.epsl.2011.09.015.

Garzione, C.N., Molnar, P., Libarkin, J.C., MacFadden, B.J., 2006. Rapid late Miocene rise of the Bolivian Altiplano: evidence for removal of mantle lithosphere. Earth Planet. Sci. Lett. 241 (3), 543–556. http://dx.doi.org/10.1016/j.epsl.2005.11.026.

Garzione, C.N., Auerbach, D.J., Jin-Sook Smith, J., Rosario, J.J., Passey, B.H., Jordan, T.E., Eiler, J.M., 2014. Clumped isotope evidence for diachronous surface cooling of the Altiplano and pulsed surface uplift of the Central Andes. Earth Planet. Sci. Lett. 393, 173–181. http://dx.doi.org/10.1016/j.epsl.2014.02.029.

Gasparini, N.M., Whipple, K.X., 2014. Diagnosing climatic and tectonic controls on topography: Eastern flank of the northern Bolivian Andes. Lithosphere L322–1. http://dx.doi.org/10.1130/L322.1.

Gesch, D., 2007. The National Elevation Dataset. In: Maune, D.F. (Ed.), Digital Elevation Model Technologies and Applications: the Dem Users Manual. Asprs Pubns.

Gesch, D., Oimoen, M., Greenlee, S., Nelson, C., Steuck, M., Tyler, D., 2002. The National Elevation Dataset. Photogramm. Eng. Remote Sens. 68 (1), 5–11.

Ghosh, P., Garzione, C.N., Eiler, J.M., 2006. Rapid uplift of the Altiplano revealed through ^{13}C–^{18}O bonds in paleosol carbonates. Science 311 (5760), 511–515. http://dx.doi.org/10.1126/science.1119365.

Goren, L., Fox, M., Willett, S.D., 2014. Tectonics from fluvial topography using formal linear inversion: theory and applications to the Inyo Mountains, California. J. Geophys. Res. Earth Surf. 1651–1681. http://dx.doi.org/10.1002/2014JF003079.

Green, P.J., 1995. Reversible jump Markov chain Monte Carlo computation and Bayesian model determination. Biometrika 82 (4), 711–732. http://dx.doi.org/10.1093/biomet/82.4.711.

Gregory-Wodzicki, K.M., 2002. A late Miocene subtropical-dry flora from the northern Altiplano, Bolivia. Palaeogeogr. Palaeoclimatol. Palaeoecol. 180 (4), 331–348. http://dx.doi.org/10.1016/S0031-0182(01)00434-5.

Hack, J.T., 1973. Stream-profile analysis and stream-gradient index. J. Res. US Geol. Surv. 1 (4), 421–429.

Harkins, N., Kirby, E., Heimsath, A., Robinson, R., Reiser, U., 2007. Transient fluvial incision in the headwaters of the Yellow River, northeastern Tibet, China. J. Geophys. Res. Earth Surf. 112 (F3). http://dx.doi.org/10.1029/2006JF000570.

Hartley, A., 2003. Andean uplift and climate change. J. Geol. Soc. 160 (1), 7–10. http://dx.doi.org/10.1144/0016-764902-083.

Hastings, W.K., 1970. Monte Carlo sampling methods using Markov chains and their applications. Biometrika 57 (1), 97–109.

Hilley, G., Coutand, I., 2010. Links between topography, erosion, rheological heterogeneity, and deformation in contractional settings: insights from the central Andes. Tectonophysics 495 (1), 78–92. http://dx.doi.org/10.1016/j.tecto.2009.06.017.

Hopcroft, P., Gallagher, K., Pain, C., 2009. A Bayesian partition modelling approach to resolve spatial variability in climate records from borehole temperature inversion. Geophys. J. Int. 178 (2), 651–666. http://dx.doi.org/10.1111/j.1365-246X.2009.04192.x.

Houseman, G.A., McKenzie, D.P., Molnar, P., 1981. Convective instability of a thickened boundary layer and its relevance for the thermal evolution of continental convergent belts. J. Geophys. Res. Solid Earth 86 (B7), 6115–6132. http://dx.doi.org/10.1029/JB086iB07p06115.

Houston, J., Hartley, A.J., 2003. The central Andean west-slope rainshadow and its potential contribution to the origin of hyper-aridity in the Atacama Desert. Int. J. Climatol. 23 (12), 1453–1464. http://dx.doi.org/10.1002/joc.938.

Howard, A.D., 1994. A detachment-limited model of drainage basin evolution. Water Resour. Res. 30 (7), 2261–2285. http://dx.doi.org/10.1029/94WR00757.

Howard, A.D., Kerby, G., 1983. Channel changes in badlands. Bull. Geol. Soc. Am. 94 (6), 739–752. http://dx.doi.org/10.1130/0016-7606(1983)94<739:CCIB>2.0.CO;2.

Husson, L., Sempere, T., 2003. Thickening the Altiplano crust by gravity-driven crustal channel flow. Geophys. Res. Lett. 30 (5). http://dx.doi.org/10.1029/2002GL016877.

Iaffaldano, G., Bodin, T., Sambridge, M., 2013. Slow-downs and speed-ups of India–Eurasia convergence since ~20 Ma: data-noise, uncertainties and dynamic implications. Earth Planet. Sci. Lett. 367, 146–156. http://dx.doi.org/10.1016/j.epsl.2013.02.014.

Insel, N., Poulsen, C.J., Ehlers, T.A., 2010. Influence of the Andes Mountains on South American moisture transport, convection, and precipitation. Clim. Dyn. 35 (7–8), 1477–1492. http://dx.doi.org/10.1007/s00382-009-0637-1.

Jarvis, A., Reuter, H.I., Nelson, A., Guevara, E., 2006. Void-filled seamless SRTM data V3, available from the CGIAR-CSI SRTM 90 m Database. http://srtm. csi. cgiar. org.

Jasra, A., Stephens, D., Gallagher, K., Holmes, C., 2006. Bayesian mixture modelling in geochronology via Markov chain Monte Carlo. Math. Geol. 38 (3), 269–300. http://dx.doi.org/10.1007/s11004-005-9019-3.

Jeffery, M.L., Ehlers, T.A., Yanites, B.J., Poulsen, C.J., 2013. Quantifying the role of paleoclimate and Andean Plateau uplift on river incision. J. Geophys. Res. Earth Surf. 118 (2), 852–871. http://dx.doi.org/10.1002/jgrf.20055.

Jordan, T., Nester, P., Blanco, N., Hoke, G., Davila, F., Tomlinson, A., 2010. Uplift of the Altiplano–Puna plateau: a view from the west. Tectonics 29 (5). http://dx.doi.org/10.1029/2010TC002661.

Kirby, E., Whipple, K., 2001. Quantifying differential rock-uplift rates via stream profile analysis. Geology 29 (5), 415–419. http://dx.doi.org/10.1130/0091-7613(2001)029<0415:QDRURV>2.0.CO;2.

Kirby, E., Whipple, K.X., 2012. Expression of active tectonics in erosional landscapes. J. Struct. Geol. 44, 54–75. http://dx.doi.org/10.1016/j.jsg.2012.07.009.

Kirby, E., Whipple, K.X., Tang, W., Chen, Z., 2003. Distribution of active rock uplift along the eastern margin of the Tibetan Plateau: inferences from bedrock channel longitudinal profiles. J. Geophys. Res. Solid Earth 108 (B4). http://dx.doi.org/10.1029/2001JB000861.

Kober, F., Ivy-Ochs, S., Schlunegger, F., Baur, H., Kubik, P., Wieler, R., 2007. Denudation rates and a topography-driven rainfall threshold in northern Chile: multiple cosmogenic nuclide data and sediment yield budgets. Geomorphology 83 (1), 97–120. http://dx.doi.org/10.1016/j.geomorph.2006.06.029.

Lague, D., 2010. Reduction of long-term bedrock incision efficiency by short-term alluvial cover intermittency. J. Geophys. Res. Earth Surf. 115 (F2). http://dx.doi.org/10.1029/2008JF001210.

Lamb, M.P., Dietrich, W.E., Sklar, L.S., 2008. A model for fluvial bedrock incision by impacting suspended and bed load sediment. J. Geophys. Res. Earth Surf. 113 (F3). http://dx.doi.org/10.1029/2007JF000915.

Lee, J., Stockli, D.F., Owen, L.A., Finkel, R.C., Kislitsyn, R., 2009. Exhumation of the Inyo Mountains, California: implications for the timing of extension along the western boundary of the Basin and Range Province and distribution of dextral fault slip rates across the eastern California shear zone. Tectonics 28 (1). http://dx.doi.org/10.1029/2008TC002295.

Lehner, B., Verdin, K., Jarvis, A., 2008. New global hydrography derived from spaceborne elevation data. EOS Trans. Am. Geophys. Union 89 (10), 93–94. http://dx.doi.org/10.1029/2008EO100001.

Luke, J.C., 1972. Mathematical models for landform evolution. J. Geophys. Res. 77 (14), 2460–2464. http://dx.doi.org/10.1029/JB077i014p02460.

Luke, J.C., 1974. Special solutions for nonlinear erosion problems. J. Geophys. Res. 79 (26), 4035–4040. http://dx.doi.org/10.1029/JB079i026p04035.

Luke, J., 1976. A note on the use of characteristics in slope evolution models. Z. Geomorphol. Suppl. 25, 114–119.

MacKay, D.J., 2003. Information Theory, Inference and Learning Algorithms. Cambridge University Press.

Malinverno, A., 2002. Parsimonious Bayesian Markov chain Monte Carlo inversion in a nonlinear geophysical problem. Geophys. J. Int. 151 (3), 675–688. http://dx.doi.org/10.1046/j.1365-246X.2002.01847.x.

Malinverno, A., Briggs, V.A., 2004. Expanded uncertainty quantification in inverse problems: hierarchical Bayes and empirical Bayes. Geophysics 69 (4), 1005–1016. http://dx.doi.org/10.1190/1.1778243.

Mudd, S.M., Attal, M., Milodowski, D.T., Grieve, S.W.D., Valters, D.A., 2014. A statistical framework to quantify spatial variation in channel gradients using the integral method of channel profile analysis. J. Geophys. Res. Earth Surf. http://dx.doi.org/10.1002/2013JF002981.

Norton, K., Schlunegger, F., 2011. Migrating deformation in the Central Andes from enhanced orographic rainfall. Nat. Commun. 2, 584. http://dx.doi.org/10.1038/ncomms1590.

Penck, W., Czech, H., Boswell, K.C., 1972. Morphological Analysis of Land Forms: a Contribution to Physical Geology. Hafner Publishing Company.

Perron, J.T., Royden, L., 2013. An integral approach to bedrock river profile analysis. Earth Surf. Process. Landf. 38, 570–576. http://dx.doi.org/10.1002/esp.3302.

Piana Agostinetti, N., Malinverno, A., 2010. Receiver function inversion by transdimensional Monte Carlo sampling. Geophys. J. Int. 181 (2), 858–872. http://dx.doi.org/10.1111/j.1365-246X.2010.04530.x.

Picard, D., Sempere, T., Plantard, O., 2008. Direction and timing of uplift propagation in the Peruvian Andes deduced from molecular phylogenetics of highland biotaxa. Earth Planet. Sci. Lett. 271 (1), 326–336. http://dx.doi.org/10.1016/j.epsl.2008.04.024.

Pingel, H., Alonso, R.N., Mulch, A., Rohrmann, A., Sudo, M., Strecker, M.R., 2014. Pliocene orographic barrier uplift in the southern Central Andes. Geology 42 (8), 691–694. http://dx.doi.org/10.1130/G35538.1.

Pope, D.C., Willett, S.D., 1998. Thermal–mechanical model for crustal thickening in the central Andes driven by ablative subduction. Geology 26 (6), 511–514. http://dx.doi.org/10.1130/0091-7613(1998)026<0511:TMMFCT>2.3.CO;2.

Poulsen, C.J., Ehlers, T.A., Insel, N., 2010. Onset of convective rainfall during gradual late Miocene rise of the central Andes. Science 328 (5977), 490–493. http://dx.doi.org/10.1126/science.1185078.

Pritchard, D., Roberts, G.G., White, N.J., Richardson, C.N., 2009. Uplift histories from river profiles. Geophys. Res. Lett. 36 (24). http://dx.doi.org/10.1029/2009GL040928.

Ray, A., Key, K., 2012. Bayesian inversion of marine CSEM data with a trans-dimensional self parametrizing algorithm. Geophys. J. Int. 191 (3), 1135–1151. http://dx.doi.org/10.1111/j.1365-246X.2012.05677.x.

Reiners, P., Thomson, S., Vernon, A., Willett, S., Zattin, M., Einhorn, J., Gehrels, G., Quade, J., Pearson, D., Murray, K., Cavazza, W., 2014. Low-temperature thermochronologic trends across the central Andes, 21°S28°S. Geol. Soc. Am. Mem. 212. http://dx.doi.org/10.1130/2015.1212(12).

Roberts, G.G., White, N., 2010. Estimating uplift rate histories from river profiles using African examples. J. Geophys. Res. 115 (B2). http://dx.doi.org/10.1029/2009JB006692 B02406.

Roberts, G., White, N., Martin-Brandis, G., Crosby, A., 2012. An uplift history of the Colorado Plateau and its surroundings from inverse modeling of longitudinal river profiles. Tectonics 31 (4). http://dx.doi.org/10.1029/2012TC003107.

Roperch, P., Sempere, T., Macedo, O., Arriagada, C., Fornari, M., Tapia, C., Garca, M., Laj, C., 2006. Counterclockwise rotation of late Eocene–Oligocene fore-arc deposits in southern Peru and its significance for oroclinal bending in the central Andes. Tectonics 25 (3). http://dx.doi.org/10.1029/2005TC001882.

Rosenbloom, N.A., Anderson, R.S., 1994. Hillslope and channel evolution in a marine terraced landscape, Santa Cruz, California. J. Geophys. Res. 99 (B7), 14013–14030. http://dx.doi.org/10.1029/94JB00048.

Rosenthal, J.S., 2000. Parallel computing and Monte Carlo algorithms. Far East J. Theor. Stat. 4 (2), 207–236.

Ross, D., 1976. Geologic map of the Waucoba Wash quadrangle, Inyo County, California. Geologic quadrangle map gq-612, scale 1:62,500, U.S. Geological Survey.

Royden, L., Perron, J.T., 2013. Solutions of the stream power equation and application to the evolution of river longitudinal profiles. J. Geophys. Res. Earth Surf. 118 (2), 497–518. http://dx.doi.org/10.1002/jgrf.20031.

Sambridge, M., Bodin, T., Gallagher, K., Tkalčić, H., 2013. Transdimensional inference in the geosciences. Philos. Trans. R. Soc. A Math. Phys. Eng. Sci. 371 (1984). http://dx.doi.org/10.1098/rsta.2011.0547.

Saylor, J.E., Horton, B.K., 2014. Nonuniform surface uplift of the Andean plateau revealed by deuterium isotopes in Miocene volcanic glass from southern Peru. Earth Planet. Sci. Lett. 387, 120–131. http://dx.doi.org/10.1016/j.epsl.2013.11.015.

Schildgen, T.F., Hodges, K.V., Whipple, K.X., Reiners, P.W., Pringle, M.S., 2007. Uplift of the western margin of the Andean plateau revealed from canyon incision history, southern Peru. Geology 35 (6), 523–526. http://dx.doi.org/10.1130/G23532A.1.

Schildgen, T.F., Ehlers, T.A., Whipp, D.M., van Soest, M.C., Whipple, K.X., Hodges, K.V., 2009. Quantifying canyon incision and Andean Plateau surface uplift, southwest Peru: a thermochronometer and numerical modeling approach. J. Geophys. Res. Earth Surf. 114 (F4). http://dx.doi.org/10.1029/2009JF001305.

Schildgen, T.F., Balco, G., Shuster, D.L., 2010. Canyon incision and knickpoint propagation recorded by apatite ^{4}He/^{3}He thermochronometry. Earth Planet. Sci. Lett. 293 (3), 377–387. http://dx.doi.org/10.1016/j.epsl.2010.03.009.

Schlunegger, F., Zeilinger, G., Kounov, A., Kober, F., Hüsser, B., 2006. Scale of relief growth in the forearc of the Andes of Northern Chile (Arica latitude, 18 S). Terra Nova 18 (3), 217–223. http://dx.doi.org/10.1111/j.1365-3121.2006.00682.x.

Schlunegger, F., Kober, F., Zeilinger, G., von Rotz, R., 2010. Sedimentology-based reconstructions of paleoclimate changes in the Central Andes in response to the uplift of the Andes, Arica region between 19 and 21 Ma latitude, northern Chile. Int. J. Earth Sci. 99 (1), 123–137. http://dx.doi.org/10.1007/s00531-010-0572-8.

Schoenbohm, L., Whipple, K., Burchfiel, B., Chen, L., 2004. Geomorphic constraints on surface uplift, exhumation, and plateau growth in the Red River region, Yunnan Province, China. Geol. Soc. Am. Bull. 116 (7–8), 895–909. http://dx.doi.org/10.1130/B25364.1.

Seidl, M.A., Dietrich, W.E., 1992. The problem of channel erosion into bedrock. Catena Suppl. 23, 101–124.

Shelef, E., Hilley, G.E., 2014. Symmetry, randomness, and process in the structure of branched channel networks. Geophys. Res. Lett. 41 (10), 3485–3493. http://dx.doi.org/10.1002/2014GL059816.

Shuster, D.L., Farley, K.A., 2004. ^{4}He/^{3}He thermochronometry. Earth Planet. Sci. Lett. 217 (1), 1–17. http://dx.doi.org/10.1016/S0012-821X(03)00595-8 (Jan.).

Sisson, S.A., 2005. Transdimensional Markov chains: a decade of progress and future perspectives. J. Am. Stat. Assoc. 100 (471), 1077–1089. http://dx.doi.org/10.1198/016214505000000664.

Sivia, D., Skilling, J., 2006. Data Analysis: a Bayesian Tutorial. Oxford University Press, USA.

Sklar, L., Dietrich, W.E., 1998. River longitudinal profiles and bedrock incision models: stream power and the influence of sediment supply. In: Tinkler, K.J., Wohl, E.E. (Eds.), Rivers Over Rock: Fluvial Processes in Bedrock Channels. American Geophysical Union, pp. 237–260 http://dx.doi.org/10.1029/GM107p0237.

Snyder, N.P., Whipple, K.X., Tucker, G.E., Merritts, D.J., 2000. Landscape response to tectonic forcing: digital elevation model analysis of stream profiles in the Mendocino triple junction region, northern California. Bull. Geol. Soc. Am. 112 (8), 1250–1263. http://dx.doi.org/10.1130/0016-7606(2000)112<1250:LRTTFD>2.0.CO;2.

Springer, M., 1999. Interpretation of heat-flow density in the Central Andes. Tectonophysics 306 (3), 377–395. http://dx.doi.org/10.1016/S0040-1951(99)00067-0.

Steffen, D., Schlunegger, F., Preusser, F., 2010. Late Pleistocene fans and terraces in the Majes valley, southern Peru, and their relation to climatic variations. Int. J. Earth Sci. 99 (8), 1975–1989. http://dx.doi.org/10.1007/s00531-009-0489-2.

Stephenson, J., Gallagher, K., Holmes, C., 2004. Beyond kriging: dealing with discontinuous spatial data fields using adaptive prior information and Bayesian partition modelling. Geol. Soc. Lond. Spec. Publ. 239 (1), 195–209. http://dx.doi.org/10.1144/GSL.SP.2004.239.01.13.

Streitz, R., Stinson, M., 1974. Geologic map of California: Death Valley sheet. scale 1:250,000, California Division of Mines and Geology.

Tarantola, A., 2005. Inverse Problem Theory and Methods for Model Parameter Estimation. SIAM.

Thouret, J.-C., Wörner, G., Gunnell, Y., Singer, B., Zhang, X., Souriot, T., 2007. Geochronologic and stratigraphic constraints on canyon incision and Miocene uplift of the Central Andes in Peru. Earth Planet. Sci. Lett. 263 (3), 151–166. http://dx.doi.org/10.1016/j.epsl.2007.07.023.

Tucker, G.E., Slingerland, R.L., 1994. Erosional dynamics, flexural isostasy, and long-lived escarpments: a numerical modeling study. J. Geophys. Res. Solid Earth 99 (B6), 12. http://dx.doi.org/10.1029/94JB00320.

Weissel, J.K., Seidl, M.A., 1998. Inland propagation of erosional escarpments and river profile evolution across the southeast Australian passive continental margin. AGU AMERICAN GEOPHYSICAL UNION vol. 107 pp. 189–206.

Wessel, P., Smith, W.H.F., 1998. New, improved version of Generic Mapping Tools released. EOS Trans. 79, 579-579.

Whipple, K., Gasparini, N., 2014. Tectonic control of topography, rainfall patterns, and erosion during rapid post–12 Ma uplift of the Bolivian Andes. Lithosphere L325–1. http://dx.doi.org/10.1130/L325.1.

Whipple, K.X., Tucker, G.E., 1999. Dynamics of the stream-power river incision model: implications for height limits of mountain ranges, landscape response timescales, and research needs. J. Geophys. Res. Solid Earth 104 (B8). http://dx.doi.org/10.1029/1999JB900120.

Whipple, K.X., Tucker, G.E., 2002. Implications of sediment-flux-dependent river incision models for landscape evolution. J. Geophys. Res. Solid Earth 107 (B2), 2039. http://dx.doi.org/10.1029/2000JB000044.

Whittaker, A.C., Boulton, S.J., 2012. Tectonic and climatic controls on knickpoint retreat rates and landscape response times. J. Geophys. Res. Earth Surf. 117 (F2). http://dx.doi.org/10.1029/2011JF002157.

Whittaker, A.C., Cowie, P.A., Attal, M., Tucker, G.E., Roberts, G.P., 2007. Bedrock channel adjustment to tectonic forcing: implications for predicting river incision rates. Geology 35 (2), 103–106. http://dx.doi.org/10.1130/G23106A.1.

Willett, S.D., McCoy, S.W., Perron, J.T., Goren, L., Chen, C.-Y., 2014. Dynamic reorganization of river basins. Science 343 (6175). http://dx.doi.org/10.1126/science.1248765.

Wobus, C.W., Crosby, B.T., Whipple, K.X., 2006. Hanging valleys in fluvial systems: controls on occurrence and implications for landscape evolution. J. Geophys. Res. Earth Surf. 111 (F2). http://dx.doi.org/10.1029/2005JF000406.

Yanites, B.J., Tucker, G.E., Hsu, H.-L., Chen, C.-c., Chen, Y.-G., Mueller, K.J., 2011. The influence of sediment cover variability on long-term river incision rates: an example from the Peikang River, central Taiwan. J. Geophys. Res. Earth Surf. 116 (F3). http://dx.doi.org/10.1029/2010JF001933.

Young, M.K., Rawlinson, N., Bodin, T., 2013. Transdimensional inversion of ambient seismic noise for 3D shear velocity structure of the Tasmanian crust. Geophysics 78 (3), WB49–WB62. http://dx.doi.org/10.1190/geo2012-0356.1.